Supplementary Information for: Physically-Derived Lindemann Melting Criterion via Lambda^3 Energy Density Ratio Theory

Masamichi Iizumi[1*]

[1*]Miosync Inc., Tokyo, Japan.

Corresponding author(s). E-mail(s): m.iizumi@miosync.email;

Contents

1 Overview, Methodology, and Conventions

1.1 Organization of Supplementary Information

This Supplementary Information (SI) document provides comprehensive technical details, data sources, fitting procedures, and statistical validation supporting the main text. The SI is organized as follows:

- **SI-2: Thermal Softening (Lambda^{s} Model)** – Data Sources and Fitting Procedures
  - Complete temperature-dependent Young's modulus $E(T)$ data for seven metals (Fe, W, Cu, Al, Ni, Ti, Mg)
  - Detailed fitting methodology for Lambda^{3} parameters (λ_{base}, κ)
  - Material-by-material validation with residual analysis
  - *Correspondence*: Main text Section 3, Figure 2, Table 1
- **SI-3: Lindemann Parameters** – Literature Compilation and Normalization
  - Experimental and theoretical Lindemann melting parameters (δ_{L}) for seven metals
  - Data provenance with complete literature references
  - Normalization procedures (lattice constant basis → nearest-neighbor basis)
  - Structure-dependent trends (BCC, FCC, HCP)
  - *Correspondence*: Main text Section 4, Table 3
- **SI-4: Born-Type Shear Collapse** and Lindemann Predictions
  - Derivation of predicted versus required shear retention factors ($f_{\text{G}}^{\text{pred}}$, $f_{\text{G}}^{\text{req}}$)
  - Structure-dependent clustering analysis
  - Born-struct rule validation (mean absolute error 5.4%)
  - Temperature evaluation sensitivity
  - *Correspondence*: Main text Section 4, Table 3
- **SI-5: EDR Regression** – Statistical Diagnostics and Validation
  - Energy-density ratio (EDR) calculation at representative temperatures
  - Through-origin regression analysis ($\delta_{\text{L}} = s\sqrt{\text{EDR}}$)
  - Leave-one-out cross-validation (LOO-CV)
  - Bootstrap confidence intervals and permutation tests
  - Model selection criteria and residual diagnostics
  - *Correspondence*: Main text Section 5, Figure 4
- **SI-6: Nanoparticle Melting-Point Depression** – Complete Dataset and Analysis
  - Experimental melting data for seven metallic nanoparticles (Au, Ag, Cu, Al, Fe, Pt, Pb)
  - Gibbs–Thomson relation validation ($1/r$ law for $r \geq 3$ nm)
  - Size-dependent coordination reduction and EDR amplification
  - Piecewise fitting procedure and statistical validation
  - *Correspondence*: Main text Section 6, Figure 5

1.2 Computational Methods and Software Environment

All numerical calculations, nonlinear fitting, and statistical analyses were performed using Python with the following environment:

1.2.1 Software versions

- Python: 3.10 or higher (tested on 3.10–3.12)
- NumPy: $\geq 1.21.0$ (array operations, mathematical functions)
- Pandas: $\geq 1.3.0$ (data manipulation, CSV I/O)
- Matplotlib: $\geq 3.4.0$ (visualization)
- SciPy: $\geq 1.7.0$ (optimization, statistical analysis)

1.2.2 Core computational methods

Nonlinear least-squares fitting (Section 2): Lambda^3 thermal-softening parameters (λ_{base}, κ) were extracted via the Levenberg–Marquardt algorithm implemented in `scipy.optimize.curve_fit`. Parameter bounds were imposed to ensure physical validity ($\lambda_{\text{base}} \in [1, 200]$, $\kappa \in [0.01, 50]$). Convergence criterion: relative tolerance 10^{-8} in parameter space.

Binary search inversion (Section 4): Required shear retention factors $f_{\text{G}}^{\text{req}}$ were determined by numerically inverting the Debye–elastic Lindemann formula. A binary search on the interval $f_{\text{G}} \in [10^{-6}, 1.0]$ was iterated until $|\delta_{\text{L,calc}} - \delta_{\text{L,exp}}| < 10^{-6}$. Typical convergence required 15–20 iterations per material.

Physical constants: All calculations used SI units with the following fundamental constants:

- Boltzmann constant: $k_{\text{B}} = 1.380\,649 \times 10^{-23}$ J/K
- Atomic mass unit: $u = 1.660\,539\,066\,60 \times 10^{-27}$ kg
- Debye approximation for phonon density of states with isotropic elasticity

Numerical stability: For materials with extreme thermal softening (Al, Mg), exponential overflow in the Lambda^3 model was mitigated by clipping the argument of $\exp[-\lambda_{\text{eff}}\alpha\Delta T]$ to a minimum of -40.

1.2.3 Reproducibility

Complete Python scripts for all calculations, including data processing, fitting, inversion, and figure generation, are available at:

GitHub repository: https://github.com/miosync-masa/lambda3-melting-criterion

All random-number-dependent procedures use fixed seeds for reproducibility.

1.3 Statistical Validation Framework

Multiple complementary statistical methods were employed to validate model predictions and assess uncertainty:

1.3.1 Leave-one-out cross-validation (LOO-CV)

Predictive stability was assessed by removing each material (or data point) in turn, refitting the model on the remaining $N - 1$ samples, and computing out-of-sample prediction error. LOO root-mean-square error ($\mathrm{RMSE}_{\mathrm{LOO}}$) quantifies generalization performance.

1.3.2 Permutation tests

Assumption-free significance testing was performed via exact permutation of material labels. Two-sided p-values quantify the probability of observing the test statistic under the null hypothesis without parametric distributional assumptions.

1.3.3 Model selection criteria

Through-origin versus intercept models were compared via Akaike Information Criterion (AIC) and uncentered R^2. Physical theory ($\delta_{\mathrm{L}} \propto \sqrt{\mathrm{EDR}}$ with zero intercept) guided model selection, supplemented by statistical diagnostics.

1.3.4 Residual diagnostics

Normality of residuals was assessed via Shapiro–Wilk and Jarque–Bera tests. Quantile-quantile (Q-Q) plots visually confirmed approximate normality, supporting parametric inference.

1.4 Notation, Symbols, and Conventions

1.4.1 Primary symbols

Lambda³ thermal-softening model (Section 2):

- $E(T)$: Young's modulus at temperature T [Pa]
- E_0: Young's modulus at reference temperature $T_0 = 300\,\mathrm{K}$ [Pa]
- λ_{base}: Baseline harmonic attenuation coefficient [dimensionless]
- κ: Anharmonicity parameter (softening acceleration) [dimensionless]
- α: Linear thermal expansion coefficient [1/K]
- T_{m}: Melting temperature [K]
- ΔT: Temperature difference $T - T_0$ [K]

Elastic moduli (Sections 2, 4):

- $G(T)$: Shear modulus at temperature T [Pa]
- $K(T)$: Bulk modulus at temperature T [Pa]
- ν: Poisson's ratio [dimensionless]
- f_{G}: Shear retention factor $G(T)/G(300\,\mathrm{K})$ [dimensionless]

Lindemann melting criterion (Sections 3, 4):

- δ_{L}: Lindemann ratio $\sqrt{\langle u^2 \rangle}/r_{\mathrm{nn}}$ [dimensionless]
- $\langle u^2 \rangle$: Mean-square atomic displacement [m^2]
- r_{nn}: Nearest-neighbor interatomic distance [m]
- T_{m}: Melting point [K]

Energy-density ratio (Section 5):

- EDR: Energy-density ratio $k_{\mathrm{B}}T/(KV_{\mathrm{atom}})$ [dimensionless]
- V_{atom}: Atomic volume [m^3]
- Λ: Dimensionless energy-density ratio $K/|V|$ [dimensionless]

Gibbs–Thomson nanoparticle melting (Section 6):

- r: Nanoparticle radius [m or nm]
- $T_{\mathrm{m}}(r)$: Size-dependent melting point [K]
- T_{m}^{∞}: Bulk melting point [K]
- ΔT_{m}: Melting-point depression $T_{\mathrm{m}}^{\infty} - T_{\mathrm{m}}(r)$ [K]
- a, b: Capillary length parameters ($1/r$ and $1/r^2$ terms) [m]
- Z: Coordination number [dimensionless]

1.4.2 Crystal structure notation

- BCC: Body-centered cubic (e.g., Fe, W)
- FCC: Face-centered cubic (e.g., Cu, Al, Ni)
- HCP: Hexagonal close-packed (e.g., Ti, Mg)

1.4.3 Statistical notation

- R^2: Coefficient of determination (uncentered for through-origin models) [dimensionless]
- RMSE: Root-mean-square error [units of dependent variable]
- CI: Confidence interval (95% unless stated otherwise)
- SE: Standard error
- LOO: Leave-one-out cross-validation

1.4.4 Unit conventions

All physical quantities are reported in SI units unless explicitly stated. Temperature is given in Kelvin [K], with Celsius [°C] provided for reference where appropriate. Atomic-scale lengths (lattice constants, interatomic distances) are reported in Ångströms [Å] for convenience, with conversions to meters [m] used in calculations.

1.5 Data Quality Assessment Criteria

Experimental and computational data sources were classified into two tiers based on measurement reliability, reproducibility, and consistency across independent studies:

1.5.1 Tier 1 (High confidence)

- Data from peer-reviewed experimental studies with explicit error bars
- Multiple independent measurements showing consistency ($< 10\%$ variation)
- Well-documented measurement techniques (ultrasonic pulse-echo, resonant ultrasound spectroscopy, X-ray/neutron diffraction, differential scanning calorimetry)
- High-purity materials ($\geq 99.9\%$ purity for elemental metals)
- Temperature-controlled environments with minimal oxidation/contamination

Examples: High-temperature elastic moduli from ultrasonic methods (Ledbetter series, Ogi et al.); nanoparticle melting from in-situ TEM with heating stage (Buffat & Borel, Zhang et al.); ab initio DFT calculations for Lindemann parameters (Kavarnadze et al., Vočadlo & Alfè).

1.5.2 Tier 2 (Moderate confidence)

- Single-source data without independent validation
- Manufacturer datasheets or engineering handbooks (ASM, NIST) where original measurement conditions are not fully specified
- Extrapolated or interpolated values from limited temperature ranges
- Molecular dynamics (MD) simulations using empirical potentials (EAM, Finnis–Sinclair) without DFT validation

1.5.3 Data exclusion criteria

Data points were excluded if:

- Measurements were performed in phase-transition regions (e.g., $\alpha \to \gamma$ transition in Fe at 1185 K, magnetic Curie points)
- Evident sample degradation (oxidation, grain growth, phase separation) during high-temperature measurements
- Inconsistency exceeding $\pm 20\%$ compared to multiple independent sources
- Nanoparticle data below $r < 2\,\mathrm{nm}$, where quantum confinement and non-bulk behavior dominate

1.5.4 Literature selection for Lindemann parameters (Section 3)

Priority was given to:

1. Recent ab initio calculations (post-2000) using DFT-based phonon theory
2. Experimental determinations via neutron/X-ray scattering (Debye–Waller factors)
3. Systematic theoretical studies with explicit structure-dependent analysis (Shapiro 1970, Kuramoto et al. 2010)

Original literature reporting δ_{L} relative to lattice constant a was converted to nearest-neighbor distance r_{nn} for consistency (e.g., FCC: $r_{\mathrm{nn}} = a/\sqrt{2}$, conversion factor $\sqrt{2} \approx 1.414$).

1.6 Code and Data Availability Statement

1.6.1 Source code

All computational scripts for data processing, Lambda^3 fitting, Lindemann predictions, EDR regression, and figure generation are available at:

GitHub repository: https://github.com/miosync-masa/lambda3-melting-criterion

The repository includes:

- Python scripts for all calculations
  - `lindemann_predictor.py` (Section 4: Born-struct predictions)
  - `gibbs_thomson_analysis.py` (Section 6: Nanoparticle analysis)
  - `lambda3_thermal_softening.py` (Section 2: Thermal softening fits)
- Requirements file (`requirements.txt`) specifying dependencies
- README with installation and usage instructions

1.6.2 Data files

All experimental and computational data used in this study are provided as CSV files in the repository `data/` directory:

1. `thermal_properties.csv` – Temperature-dependent $E(T)$, $\sigma_y(T)$, $\alpha(T)$ for 7 metals (Section 2)
2. `material_summary.csv` – Lambda^3 fitted parameters (λ_{base}, κ) and material properties (Section 2)
3. `lindemann_parameters_literature.csv` – Experimental δ_{L} values with literature sources (Section 3)
4. `lindemann_physical_results.csv` – Born-struct predictions and validation (Section 4)
5. `nanoparticle_melting_gibbs_thomson.csv` – Size-dependent melting data for 7 materials (Section 6)

1.6.3 Persistent archival

Upon acceptance, a snapshot of the repository will be archived on Zenodo with a citable DOI.

1.6.4 Correspondence

Requests for additional data or clarification should be directed to Masamichi Iizumi (Miosync Inc.): `m.iizumi@miosync.email`

1.6.5 License

All code and data are released under the MIT License, permitting unrestricted use with attribution.

2 Thermal Softening (Lambda^3 Model): Data Sources and Fitting Procedures

2.1 Overview

This section provides complete documentation of the temperature-dependent material properties and fitting procedures used to derive the Lambda^3 thermal softening parameters reported in Table 1 (main text). The Lambda^3 model describes Young's modulus evolution as:

$$E(T) = E_0 \exp\left[-\lambda_{\text{eff}}(T)\alpha\Delta T\right] \tag{1}$$

where the effective softening coefficient includes nonlinear thermal acceleration:

$$\lambda_{\text{eff}}(T) = \lambda_{\text{base}}\left(1 + \kappa\frac{\Delta T}{1000}\right) \tag{2}$$

2.1.1 Purpose of this section

- Document all input data ($\alpha(T)$, $E(T)$) with complete provenance
- Describe fitting algorithm ensuring reproducibility
- Validate model accuracy across seven metals (BCC, FCC, HCP)
- Address data quality limitations (Mg case study)

2.1.2 What this section does NOT claim

- Universal scaling laws for κ (material-specific parameters)
- Predictive formulas beyond fitted materials
- Extrapolation to unmeasured temperature ranges

All fitted parameters reproduce experimental data with residuals $< 3\%$.

2.2 Temperature-Dependent Input Data

2.2.1 Data Quality and Provenance

Temperature-dependent Young's modulus $E(T)$ and thermal expansion coefficient $\alpha(T)$ were compiled from peer-reviewed experimental studies. Data selection criteria:

1. Temperature range: 300 K to $\geq 0.5T_{\text{m}}$ (minimum 5 data points)
2. Measurement techniques:
   - $E(T)$: Ultrasonic pulse-echo, resonant ultrasound spectroscopy, or nanoindentation
   - $\alpha(T)$: Dilatometry or X-ray diffraction
3. Material purity: $\geq 99.9\%$ for elemental metals
4. Reproducibility: Multiple independent studies when available

2.2.2 Material Properties Summary

Complete temperature-dependent data for seven metals are provided in `data/thermal_properties.csv`. Table 1 summarizes baseline properties at room temperature.

Table 1 Baseline material properties at 300 K for seven elemental metals.

Material	Structure	T_m [K]	a_0 [Å]	E_0 [GPa]	ν	α [10^{-6} K^{-1}]	α/T_m [10^{-9} K^{-2}]
Fe	BCC	1811	2.92	211	0.29	15.0	8.28
W	BCC	3695	3.16	411	0.28	4.3	1.16
Cu	FCC	1357	3.61	130	0.34	17.0	12.53
Al	FCC	933	4.05	70	0.35	23.0	24.65
Ni	FCC	1728	3.52	200	0.31	13.3	7.70
Ti	HCP	1941	2.95	116	0.32	8.6	4.43
Mg	HCP	923	3.21	45	0.29	26.0	28.17

Notes:

- a_0: Lattice constant at 300 K
- E_0: Young's modulus at 300 K
- ν: Poisson's ratio (weakly temperature-dependent)
- α: Linear thermal expansion coefficient (average over measured range)

2.3 Material-by-Material Data Tables

2.3.1 Table SI-2.1: Iron (Fe) — BCC

Material properties:

- Structure: BCC (α-Fe at RT; δ-Fe near melting after FCC γ-phase)
- $T_m = 1811$ K (1538 °C)
- $E_0 = 210$ GPa (at 300 K)
- $\alpha = 15.0 \times 10^{-6}$ K^{-1} (average 300–1200 K)
- Poisson's ratio: $\nu = 0.29$

Data notes:

- Phase transition: $\alpha \rightarrow \gamma$ (BCC→FCC) at 1185 K excluded from fit
- Magnetic transition (Curie point 1043 K) induces minor anomaly, negligible for fitting
- δ-Fe (BCC) melts at 1811 K; data limited to < 1200 K (α-phase)

Table 2 Temperature-dependent properties for Iron (Fe, BCC).

T [K]	E [GPa]	σ_y [MPa]	α [$\times 10^{-6}$ K^{-1}]	Reference
300	210	300	14.8	[1]
500	180	250	15.2	[1]
800	127	150	16.0	[2]
1000	100	50	16.5	[2]
1180	80	20	17.2	[3]

2.3.2 Table SI-2.2: Copper (Cu) — FCC

Material properties:

- Structure: FCC (stable to melting)
- $T_\mathrm{m} = 1357\,\mathrm{K}$ (1085 °C)
- $E_0 = 130\,\mathrm{GPa}$ (at 300 K)
- $\alpha = 17.0 \times 10^{-6}$ K^{-1} (average 300–1100 K)
- Poisson's ratio: $\nu = 0.34$

Table 3 Temperature-dependent properties for Copper (Cu, FCC).

T [K]	E [GPa]	σ_y [MPa]	α [$\times 10^{-6}$ K^{-1}]	Reference
300	130	70	16.5	[4]
500	115	55	17.2	[4]
700	95	35	18.0	[5]
900	75	15	19.2	[5]
1100	55	5	20.8	[6]

Data notes:

- High-purity OFHC (Oxygen-Free High Conductivity) copper
- No phase transitions; smooth softening throughout
- Low cohesive energy → strong thermal softening ($\kappa = 1.713$, Table 1)

2.3.3 Table SI-2.3: Aluminum (Al) — FCC

Material properties:

- Structure: FCC (stable to melting)
- $T_\mathrm{m} = 933\,\mathrm{K}$ (660 °C)
- $E_0 = 69\,\mathrm{GPa}$ (at 300 K)
- $\alpha = 23.0 \times 10^{-6}$ K^{-1} (average 300–800 K)

- Poisson's ratio: $\nu = 0.35$

Table 4 Temperature-dependent properties for Aluminum (Al, FCC).

T [K]	E [GPa]	σ_y [MPa]	α [$\times 10^{-6}$ K^{-1}]	Reference
300	69	30	23.1	[7]
400	62	24	24.0	[7]
500	54	18	25.2	[8]
600	45	12	26.8	[8]
700	35	6	28.5	[9]
800	25	2	30.5	[9]

Data notes:

- 99.99% purity Al (commercial grade)
- Extreme thermal softening: 64% E loss from 300–800 K
- Highest nonlinearity: $\kappa = 4.180$ (tied with Mg)
- Lowest cohesive energy among FCC metals studied

2.3.4 Table SI-2.4: Nickel (Ni) — FCC

Material properties:

- Structure: FCC (stable to melting)
- $T_\mathrm{m} = 1728\,\mathrm{K}$ (1455 °C)
- $E_0 = 205\,\mathrm{GPa}$ (at 300 K)
- $\alpha = 13.3 \times 10^{-6}$ K^{-1} (average 300–1273 K)
- Poisson's ratio: $\nu = 0.31$

Table 5 Temperature-dependent properties for Nickel (Ni, FCC).

T [K]	E [GPa]	σ_y [MPa]	α [$\times 10^{-6}$ K^{-1}]	Reference
299	205	110	13.0	[10]
373	200	170	13.2	[10]
473	192	115	13.5	[10]
644	180	85	14.0	[11]
773	177	65	14.3	[11]
1000	160	40	15.0	[12]
1273	140	20	16.2	[12]

Data notes:

- High-purity Ni (99.98%)
- Strong d-electron bonding → near-harmonic behavior ($\kappa = 0.279$, lowest among FCC)
- Magnetic ordering (Curie point 631 K) induces minor anomaly at 644 K
- Most temperature-stable FCC metal in dataset

2.3.5 Table SI-2.5: Titanium (Ti) — HCP

Material properties:

- Structure: HCP (α-Ti, RT to 1155 K); BCC (β-Ti, 1155 K to $T_\mathrm{m} = 1941$ K)
- $T_\mathrm{m} = 1941$ K (1668 °C)
- $E_0 = 116$ GPa (at 300 K, α-phase)
- $\alpha = 8.6 \times 10^{-6}$ K^{-1} (average 300–873 K, α-phase)
- $c/a = 1.587$ (close to ideal HCP 1.633)
- Poisson's ratio: $\nu = 0.32$

Table 6 Temperature-dependent properties for Titanium (Ti, HCP).

T [K]	E [GPa]	σ_y [MPa]	α [$\times 10^{-6}$ K^{-1}]	Reference
300	116	300	8.6	[13]
373	112	170	8.8	[13]
473	108	115	9.0	[2]
573	102	80	9.3	[2]
873	85	50	10.2	[14]

Data notes:

- Data limited to α-HCP phase (< 1155 K) to avoid phase transition complexity
- β-Ti (BCC) melting point 1941 K; Lindemann parameter quoted for α-phase
- Low thermal expansion → moderate softening ($\kappa = 0.771$)
- Ti-6Al-4V alloy data excluded; only commercial-purity (CP) Ti used

2.3.6 Table SI-2.6: Tungsten (W) — BCC

Material properties:

- Structure: BCC (stable throughout to melting)
- $T_\mathrm{m} = 3695$ K (3422 °C) — highest melting point of all elements
- $E_0 = 400$ GPa (at 300 K)
- $\alpha = 4.3 \times 10^{-6}$ K^{-1} (average 300–2000 K)

- Poisson's ratio: $\nu = 0.28$

Table 7 Temperature-dependent properties for Tungsten (W, BCC).

T [K]	E [GPa]	σ_y [MPa]	α [$\times 10^{-6}$ K^{-1}]	Reference
293	400	500	4.3	[15]
500	390	480	4.4	[15]
800	370	450	4.5	[16]
1073	360	500	4.6	[16]
1273	340	300	4.7	[17]
1473	320	300	4.9	[17]
2000	250	150	5.3	[18]

Data notes:

- Highest E_0 and T_m in dataset
- Minimal thermal expansion ($\alpha = 4.3 \times 10^{-6}$ K^{-1}, lowest in study)
- Despite low α, exhibits significant nonlinearity ($\kappa = 2.759$)
- Strong d-d bonding maintains cohesion to extreme temperatures
- BCC structure throughout; no phase transitions

2.3.7 Table SI-2.7: Magnesium (Mg) — HCP

Material properties:

- Structure: HCP (stable to melting)
- $T_\mathrm{m} = 923\,\mathrm{K}$ (650 °C)
- $E_0 = 45\,\mathrm{GPa}$ (at 300 K)
- $\alpha = 26.0 \times 10^{-6}$ K^{-1} (average 300–673 K)
- $c/a = 1.624$ (slightly above ideal HCP)
- Poisson's ratio: $\nu = 0.29$

Data notes:

- Extreme thermal softening: 67% E loss from 300–673 K (most severe in dataset)
- Highest α/T_m ratio (28.2×10^{-9} K^{-2})
- Weak cohesion + high thermal expansion → maximum nonlinearity ($\kappa = 4.186$)
- Numerical challenges in unconstrained fitting (Section 2.5)

Table 8 Temperature-dependent properties for Magnesium (Mg, HCP).

T [K]	E [GPa]	σ_y [MPa]	α [$\times 10^{-6}$ K^{-1}]	Reference
300	45	200	25.2	[19]
373	42	150	26.0	[19]
473	35	100	27.5	[8]
573	23	50	29.0	[8]
673	15	20	30.8	[20]

2.4 Fitting Methodology

2.4.1 Nonlinear Least-Squares Algorithm

Parameters (λ_{base}, κ) were extracted by minimizing the residual sum of squares:

$$\text{RSS} = \sum_{i=1}^{N} \left[E_{\text{norm}}(T_i) - E_{\text{model}}(T_i; \lambda_{\text{base}}, \kappa)\right]^2 \tag{3}$$

where normalized Young's modulus:

$$E_{\text{norm}}(T) = \frac{E(T)}{E(300\,\text{K})} \tag{4}$$

and model prediction:

$$E_{\text{model}}(T; \lambda_{\text{base}}, \kappa) = \exp\left[-\lambda_{\text{eff}}(T)\alpha(T - 300\,\text{K})\right] \tag{5}$$

$$\lambda_{\text{eff}}(T) = \lambda_{\text{base}}\left(1 + \kappa\frac{T - 300}{1000}\right) \tag{6}$$

2.4.2 Implementation

- Algorithm: Levenberg-Marquardt (`scipy.optimize.curve_fit`)
- Initial guess: $\lambda_{\text{base}} = 50$, $\kappa = 1.0$
- Bounds: $\lambda_{\text{base}} \in [1, 200]$, $\kappa \in [0.01, 10]$ (standard materials); Mg: $\kappa \in [0.01, 50]$
- Convergence: Relative tolerance 10^{-8} in parameter space
- Maximum iterations: 10,000 (typically converges in < 100)

2.4.3 Standard error estimation

Parameter uncertainties computed from covariance matrix diagonal:

$$\sigma_\lambda = \sqrt{\text{Cov}[\lambda_{\text{base}}, \lambda_{\text{base}}]}, \quad \sigma_\kappa = \sqrt{\text{Cov}[\kappa, \kappa]} \tag{7}$$

Reported as $\pm 1\sigma$ (68% confidence interval).

2.4.4 Residual metric

Mean absolute percentage error (MAPE):

$$\text{Residual} = \frac{1}{N}\sum_{i=1}^{N}\left|\frac{E_{\text{model}}(T_i) - E_{\text{exp}}(T_i)}{E_{\text{exp}}(T_i)}\right| \times 100\% \tag{8}$$

Target: Residual $< 3\%$ for acceptable fit quality.

2.5 Magnesium: Limited Data Coverage and Parameter Uncertainty

2.5.1 Extreme Material Properties

Mg represents the most challenging case in our dataset due to combined extreme characteristics:

Thermal characteristics:

- Highest α/T_{m} ratio (28.2×10^{-9} K^{-2}, 70% above Al)
- Lowest melting point (923 K, minimum in dataset)
- Most severe softening (67% E loss from 300–673 K)
- Lowest cohesive energy among HCP metals (1.51 eV/atom vs. 4.85 eV/atom for Ti)

Experimental challenges:

- Chemical reactivity: MgO surface layer formation ($E_{\text{MgO}} \approx 300$ GPa) requires inert atmosphere for high-T measurements
- Limited data availability: Only 5 temperature points vs. 7 for well-characterized metals (Ni, W)
- Measurement scatter: Oxidation artifacts and sample handling difficulties amplify uncertainty
- Temperature range limitation: $T_{\text{max}} = 673\,\text{K} = 0.73T_{\text{m}}$ (measurements beyond $0.75T_{\text{m}}$ are experimentally impractical due to severe oxidation and creep onset)

2.5.2 Fitted Parameters and Uncertainty

Unconstrained optimization with bounds $\lambda \in [1, 200]$, $\kappa \in [0.01, 50]$:

Results:

- $\lambda_{\text{base}} = 7.5 \pm 7.9$ (SE/$\lambda = 105\%$)
- $\kappa = 37.6 \pm 43.2$ (SE/$\kappa = 115\%$)
- Residual = 2.1%

Parameter correlation:

- Strong λ-κ correlation ($\rho > 0.95$)
- Multiple (λ, κ) pairs reproduce $E(T)$ within experimental uncertainty

- Large standard errors (SE > parameter value) indicate high parameter uncertainty

2.5.3 Physical Interpretation

Despite statistical uncertainty, the large κ value has physical basis:

1. **Consistent with material trends:** Among all materials, Al shows highest $\kappa = 4.18$ for $\alpha/T_m = 24.65$. Mg's $\alpha/T_m = 28.17$ (14% higher) naturally corresponds to larger κ.
2. **Anharmonicity indicators:** Lowest T_m (923 K), weakest cohesion ($E_0 = 45$ GPa), and highest thermal expansion ($\alpha = 26 \times 10^{-6}$ K^{-1}) all point to extreme phonon anharmonicity.
3. **Model validity maintained:** Despite parameter uncertainty, the Lambda^3 functional form accurately reproduces $E(T)$ evolution (residual 2.1%), confirming the exponential-with-acceleration framework captures Mg's thermal softening.

2.5.4 Implications for Lambda^8 Framework

Mg demonstrates both strengths and limitations of the empirical fitting approach:

Strengths:

- Lambda^3 model successfully describes even the most extreme material
- Functional form robust across 4× range in T_m, 9× range in E_0
- Residual quality (2.1%) comparable to data-rich materials

Limitations:

- Sparse data ($N = 5$, $T_{max} = 0.73T_m$) precludes precise parameter extraction
- High-temperature measurements prevented by oxidation and creep
- Parameter values should be treated as order-of-magnitude estimates rather than precise fitted constants

For practical applications:

- Mg's $E(T)$ predictions: use with caution, ±20–30% uncertainty
- Comparative analysis: Mg demonstrates boundary of empirical fitting reliability
- Future work: Ab initio phonon calculations or molecular dynamics simulations could provide complementary constraints beyond experimental temperature range

This case underscores the importance of transparent uncertainty reporting in materials modeling: fitted parameters are not always equally reliable, and honest assessment of data quality is essential for scientific integrity.

2.6 Fitted Parameters and Validation

Table 9 summarizes the fitted Lambda^3 parameters for all seven materials.

Table 9 Summary of Lambda³ fitted parameters for seven elemental metals. Standard errors (SE) represent $\pm 1\sigma$ confidence intervals from covariance matrix.

Material	Structure	λ_{base}	SE	κ	SE	Residual [%]	α/T_{m} [10^{-9} K^{-2}]
Fe	BCC	49.2	4.4	0.573	0.195	1.5	8.28
W	BCC	10.9	4.4	2.759	1.562	1.1	1.16
Cu	FCC	26.3	1.1	1.713	0.129	0.3	12.53
Al	FCC	27.3	2.2	4.180	0.706	1.1	24.65
Ni	FCC	22.6	2.2	0.279	0.155	0.8	7.70
Ti	HCP	43.1	2.4	0.771	0.156	0.3	4.43
Mg†	HCP	7.5	7.9	37.568	43.215	2.1	28.17

† **Magnesium caveat:** Large standard errors ($\text{SE}_\kappa/\kappa = 115\%$, $\text{SE}_\lambda/\lambda = 105\%$) indicate high parameter uncertainty due to limited data ($N = 5$, $T_{\max} = 0.73T_{\text{m}}$). Fitted values are order-of-magnitude estimates; use with caution in quantitative predictions.

2.6.1 Fit Quality Assessment

Overall performance:

- Mean residual: 1.1% (excellent agreement)
- All materials: residual $< 2.5\%$
- Best fits: Cu, Ti (0.3%) — minimal scatter, high data quality
- Acceptable fits: Fe, Mg (1.5%, 2.1%) — larger scatter but model valid

Structure-dependent trends:

Table 10 Structure-wise statistics for Lambda³ fitted parameters.

Structure	Mean λ_{base}	Mean κ	Mean Residual [%]	N
BCC	30.0 ± 19.1	1.67 ± 1.09	1.3 ± 0.2	2
FCC	25.4 ± 2.0	2.06 ± 1.61	0.7 ± 0.3	3
HCP‡	25.3 ± 17.8	19.17 ± 18.40	1.2 ± 0.9	2

‡ HCP variance note: Large scatter dominated by Mg uncertainty. Ti alone shows well-determined parameters ($\lambda = 43.1 \pm 2.4$, $\kappa = 0.771 \pm 0.156$).

Observations:

- FCC metals show tightest clustering (CV = 8% for λ), reflecting similar bonding environments

- BCC metals span widest range (Fe: 49.2, W: 10.9), consistent with diverse T_m (1811–3695 K)
- HCP statistics influenced by Mg outlier; excluding Mg would yield more representative values

2.6.2 Per-Material Fit Validation

Individual material fits are shown in Figure 2 (main text). Table 11 summarizes the validation metrics for each material.

Table 11 Validation metrics by material.

Material	N points	T range [K]	R^2	Max error [%]	RMSE [GPa]
Fe	5	300–1180	0.992	2.8	3.5
Cu	5	300–1100	0.998	0.6	1.4
Al	6	300–800	0.997	1.9	1.0
Ni	7	299–1273	0.996	1.5	1.7
Ti	5	300–873	0.999	0.5	0.7
W	7	293–2000	0.995	2.1	4.2
Mg	5	300–673	0.996	2.3	0.6

All materials achieve $R^2 > 0.99$, confirming excellent model-data agreement.

2.7 Parameter Diversity Across Materials

2.7.1 Material-Specific Parameters

The Lambda[3] parameters (λ_{base}, κ) are material-specific fitted constants, reflecting each metal's unique combination of:

- Cohesive energy (bond strength)
- Crystal structure (coordination, slip systems)
- Electronic structure (d-band contributions for transition metals)
- Anharmonicity (phonon–phonon coupling strength)

2.7.2 Key Findings from Table 9

λ_{base} variation:

- Range: 7.5 (Mg) to 49.2 (Fe) — factor of 6.6×
- BCC metals: 10.9–49.2 (extreme range)
- FCC metals: 22.6–27.3 (tight clustering, CV = 8%)
- Physical basis: $\lambda_{base} \propto$ anharmonic coupling strength

κ variation:

- Range: 0.28 (Ni) to 37.6 (Mg) — factor of 134×
- Reflects acceleration of softening near T_m
- No simple predictive formula from bulk properties
- Requires direct fitting to $E(T)$ data

2.7.3 Structure-Dependent Trends

While materials of the same crystal structure show some similarity in parameter ranges, within-structure variance remains substantial:

- BCC: $\lambda = 30.0 \pm 19.1$, $\kappa = 1.67 \pm 1.09$
- FCC: $\lambda = 25.4 \pm 2.0$, $\kappa = 2.06 \pm 1.61$
- HCP: $\lambda = 25.3 \pm 17.8$, $\kappa = 19.2 \pm 18.4$ (Mg-dominated)

2.7.4 Conclusion

Each material requires individual fitting to experimental $E(T)$ data. No universal scaling law relates (λ_{base}, κ) to simple bulk properties (α, T_m, E_0). The Lambda^3 framework provides a functional form; parameters capture material-specific physics.

3 Lindemann Parameters: Literature Compilation and Normalization

3.1 Overview

This section provides comprehensive documentation of experimental Lindemann melting parameters (δ_L) for seven metals used in our analysis (Section 4, main text). The Lindemann criterion[21] states that melting occurs when the root-mean-square atomic vibration amplitude reaches a critical fraction of the interatomic spacing:

$$\delta_L \equiv \frac{\sqrt{\langle u^2 \rangle}}{r_{nn}} \approx 0.10\text{–}0.18 \quad (\text{at } T_m) \tag{9}$$

3.1.1 Key challenges addressed

1. **Definition ambiguity:** Literature reports δ_L relative to different reference lengths (nearest-neighbor distance r_{nn} vs. lattice constant a)
2. **Method diversity:** Values derived from theoretical models, neutron scattering, MD simulations, or empirical fits
3. **Temperature conditions:** Some studies report δ at $T < T_m$, requiring extrapolation

We compile original literature values, normalize to consistent r_{nn} basis, and provide complete provenance for reproducibility.

3.2 Definition and Normalization

3.2.1 Standard Definition (This Work)

$$\boxed{\delta_L = \frac{\sqrt{\langle u^2 \rangle}}{r_{nn}}} \tag{10}$$

where r_{nn} is the nearest-neighbor atomic distance at temperature T (accounting for thermal expansion).

3.2.2 Alternative Definitions in Literature

Some studies report δ relative to lattice constant a:

$$\delta_L^{(a)} = \frac{\sqrt{\langle u^2 \rangle}}{a} \tag{11}$$

Conversion factors:

Example: Shapiro (1970)[22] reported $\delta_L^{(a)} \approx 0.071$ for FCC metals (Cu, Al). Converting to r_{nn} basis:

$$\delta_L^{(r_{nn})} = 0.071 \times \sqrt{2} \approx 0.100 \tag{12}$$

This matches the canonical "10% rule" for FCC structures.

Table 12 Conversion factors from lattice-constant basis to nearest-neighbor basis.

Structure	r_{nn} in terms of a	Conversion: $\delta_{\mathrm{L}}^{(a)} \to \delta_{\mathrm{L}}^{(r_{\mathrm{nn}})}$
BCC	$r_{\mathrm{nn}} = (\sqrt{3}/2)a \approx 0.866a$	$\delta_{\mathrm{L}} = \delta_{\mathrm{L}}^{(a)}/0.866 \approx 1.15 \times \delta_{\mathrm{L}}^{(a)}$
FCC	$r_{\mathrm{nn}} = a/\sqrt{2} \approx 0.707a$	$\delta_{\mathrm{L}} = \delta_{\mathrm{L}}^{(a)}/0.707 \approx 1.41 \times \delta_{\mathrm{L}}^{(a)}$
HCP	$r_{\mathrm{nn}} \approx a$ (basal)	$\delta_{\mathrm{L}} = \delta_{\mathrm{L}}^{(a)} \times (a/r_{\mathrm{nn}}) \approx 1.00 \times \delta_{\mathrm{L}}^{(a)}$

3.3 Material-by-Material Compilation

Complete literature values for all seven metals are provided in `data/lindemann_parameters_literature.csv`. Table 13 summarizes the adopted values with primary sources.

Table 13 Experimental Lindemann parameters for seven elemental metals with literature sources. All values normalized to r_{nn} basis.

Material	Structure	T_{m} [K]	δ_{L}	Method	Primary Source
Fe	BCC	1811	0.180	Phonon instability model	Kuramoto et al. (2010)[23]
W	BCC	3695	0.160	Lindemann rule + EOS	Minakov & Levashov (2015)[24]
Cu	FCC	1357	0.100	Lattice dynamics (converted)	Shapiro (1970)[22]
Al	FCC	933	0.100	Lattice dynamics (converted)	Shapiro (1970)[22]
Ni	FCC	1728	0.110	Lattice dynamics (converted)	Shapiro (1970)[22]
Ti	HCP	1941	0.100	Lindemann criterion (Debye)	Vopson et al. (2020)[25]
Mg	HCP	923	0.117	First-principles/MD	Kavarnadze et al. (2023)[26]

3.4 Material-by-Material Literature Compilation

3.4.1 SI-3.3.1 Iron (Fe) — BCC

Adopted value: $\delta_{\mathrm{L}} = 0.180$ (18%)

Table 14 Literature compilation for Iron (Fe, BCC).

Source	Method	Definition	Original Value	T Condition	Normalized δ_{L}
Kuramoto et al. (2010)[23]	Phonon instability model	r_{nn}	0.183	T_{m} (1811 K)	0.180
Lawson (2009)[27]	Quantum Lindemann	r_{nn}	0.16–0.18	T_{m}	0.17 (midpoint)
Vopson et al. (2020)[25]	General BCC	r_{nn}	∼0.18	T_{m}	0.18

Assessment:

- Excellent consistency across methods (phonon theory, quantum corrections, empirical)
- Range: 0.16–0.183 (14% spread)
- Adopted: 0.180 (rounded mean, consistent with BCC structure expectation)

Material properties:

- Structure: BCC (α-Fe at $T < 1185\,\mathrm{K}$; δ-Fe near melting)
- $T_\mathrm{m} = 1811\,\mathrm{K}$ (1538 °C)
- Note: Fe undergoes $\alpha \to \gamma$ (BCC→FCC) at 1185 K, then $\gamma \to \delta$ (FCC→BCC) at 1667 K before melting from δ-BCC phase

3.4.2 SI-3.3.2 Tungsten (W) — BCC

Adopted value: $\delta_\mathrm{L} = 0.160$ (16%)

Table 15 Literature compilation for Tungsten (W, BCC).

Source	Method	Definition	Original Value	T Condition	Normalized δ_L
Minakov & Levashov (2015)[24]	Lindemann rule + EOS	r_nn	0.15–0.16	T_m (3695 K)	0.160
Kuramoto et al. (2010)[23]	BCC general	r_nn	0.183 (BCC avg)	T_m	0.183
Gilvarry (1956)[28]	Empirical BCC	r_nn	∼0.15	T_m	0.15

Assessment:

- Moderate spread: 0.15–0.183 (22% variation)
- Lower than Fe despite same BCC structure → reflects stronger bonding ($T_\mathrm{m} = 3695\,\mathrm{K}$, highest of all elements)
- Adopted: 0.160 (mid-range, excludes outlier 0.183)

Material properties:

- Structure: BCC (stable throughout to melting)
- $T_\mathrm{m} = 3695\,\mathrm{K}$ (3422 °C) — highest melting point of all metals
- Extreme hardness: Minimal thermal expansion ($\alpha = 4.5 \times 10^{-6}\ \mathrm{K}^{-1}$)

3.4.3 SI-3.3.3 Copper (Cu) — FCC

Adopted value: $\delta_\mathrm{L} = 0.100$ (10%)

Assessment:

- Excellent agreement: 0.092–0.105 (14% spread)
- Shapiro's a-basis value (0.071) converts to 0.100 via $\sqrt{2}$ factor — matches empirical and MD

Table 16 Literature compilation for Copper (Cu, FCC).

Source	Method	Definition	Original Value	T Condition	Normalized δ_{L}
Shapiro (1970)[22]	Lattice dynamics	a	0.071	T_{m} (1358 K)	0.100
Gilvarry (1956)[28]	FCC empirical	r_{nn}	0.10	T_{m}	0.10
Jin et al. (2001)[29]	MD simulation	r_{nn}	0.092–0.105	T_{m}	0.099 (mean)

- Adopted: 0.100 (canonical FCC value)

Material properties:

- Structure: FCC (stable to melting)
- $T_{\mathrm{m}} = 1358\,\mathrm{K}$ (1085 °C)
- Highly ductile, low cohesive energy → rapid thermal softening

3.4.4 SI-3.3.4 Aluminum (Al) — FCC

Adopted value: $\delta_{\mathrm{L}} = 0.100$ (10%)

Table 17 Literature compilation for Aluminum (Al, FCC).

Source	Method	Definition	Original Value	T Condition	Normalized δ_{L}
Shapiro (1970)[22]	Lattice dynamics	a	0.071	T_{m} (933 K)	0.100
Vočadlo & Alfè (2002)[30]	Ab initio MD	r_{nn}	0.095–0.105	T_{m}	0.100 (mean)
Sun & Simon (2007)[31]	Nanoparticle DSC	r_{nn}	0.09–0.11	T_{m} (bulk)	0.10

Assessment:

- Canonical FCC agreement: 0.095–0.105 across all methods
- Shapiro's universal FCC value (0.071 on a-basis) confirmed by modern DFT
- Adopted: 0.100 (FCC standard)

Material properties:

- Structure: FCC (stable to melting)
- $T_{\mathrm{m}} = 933\,\mathrm{K}$ (660 °C)
- Lowest cohesive energy among FCC metals → extreme softening ($\kappa = 4.18$, Table 1 main text)

3.4.5 SI-3.3.5 Nickel (Ni) — FCC

Adopted value: $\delta_{\mathrm{L}} = 0.110$ (11%)

Assessment:

Table 18 Literature compilation for Nickel (Ni, FCC).

Source	Method	Definition	Original Value	T Condition	Normalized δ_L
Shapiro (1970)[22]	Lattice dynamics (extrap.)	a	0.078	T_m (1728 K)	0.110
Ross & McMahan (1982)[32]	High-P theory	r_{nn}	0.11–0.12	T_m (0 GPa)	0.115
Alfè (2009)[33]	DFT-MD	r_{nn}	0.105–0.115	T_m	0.110

- Slightly higher than Cu/Al: 0.105–0.115 (reflects higher T_m, stronger bonding)
- Shapiro noted Ni "deviated from FCC average" (0.071 → 0.078 on a-basis)
- Converts to 0.110 on r_{nn} basis, matching DFT
- Adopted: 0.110 (Ni-specific FCC value)

Material properties:

- Structure: FCC (stable to melting)
- $T_m = 1728\,\mathrm{K}$ (1455 °C) — highest T_m among FCC in this study
- Strong d-electron bonding → near-harmonic behavior ($\kappa = 0.267$, Table 1)

3.4.6 SI-3.3.6 Titanium (Ti) — HCP

Adopted value: $\delta_L = 0.100$ (10%)

Table 19 Literature compilation for Titanium (Ti, HCP).

Source	Method	Definition	Original Value	T Condition	Normalized δ_L
Vopson et al. (2020)[25]	Debye + Lindemann	r_{nn}	∼0.10	T_m (1941 K)	0.100
Morris et al. (2002)[34]	Embedded atom MD	r_{nn}	0.095–0.105	T_m (β-Ti)	0.100
General HCP rule		r_{nn}	0.10	T_m	0.10

Assessment:

- Consistent with general HCP threshold (∼10%)
- Phase complexity: α-Ti (HCP) → β-Ti (BCC) at 1155 K; melts from β-BCC at T_m
- Lindemann parameter typically quoted for α-HCP phase
- Adopted: 0.100 (HCP baseline)

Material properties:

- Structure: HCP (α-phase, RT to 1155 K); BCC (β-phase, 1155 K to $T_m = 1941\,\mathrm{K}$)
- $T_m = 1941\,\mathrm{K}$ (1668 °C)
- $c/a = 1.587$ (close to ideal 1.633)
- Low thermal expansion ($\alpha = 8.6 \times 10^{-6}\ \mathrm{K}^{-1}$) → thermal stability

3.4.7 SI-3.3.7 Magnesium (Mg) — HCP

Adopted value: $\delta_L = 0.117$ (11.7%)

Table 20 Literature compilation for Magnesium (Mg, HCP).

Source	Method	Definition	Original Value	T Condition	Normalized δ_L
Kavarnadze et al. (2023)[26]	Ab initio (DFT)	r_{nn}	0.117	T_m (923 K)	0.117
Vopson et al. (2020)[25]	HCP general	r_{nn}	∼0.10	T_m	0.10
Alavi & Thompson (2006)[35]	MD simulation	r_{nn}	0.11–0.12	T_m	0.115

Assessment:

- Higher than Ti: 0.117 vs. 0.100 (reflects weaker bonding, lower T_m)
- Kavarnadze's DFT value (0.117) is most rigorous recent determination
- Slightly exceeds "canonical" HCP 0.10, consistent with weak cohesion
- Adopted: 0.117 (DFT benchmark)

Material properties:

- Structure: HCP (stable to melting)
- $T_m = 923\,\mathrm{K}$ (650 °C) — lowest T_m in study
- $c/a = 1.624$ (slightly above ideal)
- Extreme thermal expansion ($\alpha = 26 \times 10^{-6}\ \mathrm{K}^{-1}$) + low cohesion → severe softening ($\kappa = 4.186$)

3.5 Structure-Dependent Trends

Table 21 summarizes Lindemann parameters by crystal structure.

Table 21 Summary of Lindemann parameters by crystal structure.

Structure	Materials	δ_L Range	Median δ_L	Mean δ_L	Std Dev	CV [%]
BCC	Fe, W	0.160–0.180	0.170	0.170	0.010	5.9
FCC	Cu, Al, Ni	0.100–0.110	0.100	0.103	0.005	4.9
HCP	Ti, Mg	0.100–0.117	0.109	0.109	0.009	8.3

3.5.1 Statistical Analysis

One-way ANOVA (structure effect on δ_L):

- F-statistic: 28.4

- p-value: 0.002
- Conclusion: Structure significantly affects δ_L ($p < 0.01$)

Post-hoc comparisons (Tukey HSD):

- BCC vs. FCC: $p = 0.003$ (significant)
- BCC vs. HCP: $p = 0.012$ (significant)
- FCC vs. HCP: $p = 0.38$ (not significant)

Interpretation:

- BCC metals require larger vibrational amplitude ($\delta \approx 0.17$) to melt, reflecting their open structure (68% packing) and geometric frustration under shear
- FCC/HCP cluster together ($\delta \approx 0.10$–0.11) due to similar close packing (74%)
- Within-structure variance is small (CV < 10%), supporting universality

3.6 Methodological Considerations

3.6.1 Experimental vs. Theoretical Determination

Table 22 Comparison of different methods for determining Lindemann parameters.

Method	Materials	Typical δ_L	Uncertainty	Advantages	Limitations
Neutron scattering	Fe, Cu, Ni	0.09–0.12	±15%	Direct $\langle u^2 \rangle$ measurement	Requires single crystals
X-ray diffraction	Al, Mg	0.08–0.11	±20%	Standard technique	Debye-Waller complex
MD simulation	All	0.09–0.12	±10%	Full T range	Potential-dependent
Phonon theory	BCC, FCC	0.10–0.18	±5%	Predictive	Requires phonon DOS
Ab initio DFT	Al, Mg	0.095–0.117	±5%	Most rigorous	Computationally expensive

Consensus approach (this work):

- **Prioritize:** Recent DFT/MD (post-2000) for direct $\langle u^2 \rangle$ at T_m
- **Cross-validate:** Compare with phonon theory (Shapiro[22], Vopson[25])
- **Avoid:** Pre-1980 empirical fits (insufficient temperature control)
- **Normalize:** Convert all to r_{nn} basis for consistency

3.7 Temperature Dependence of δ_L

3.7.1 Implicit Assumption

All reported δ_L values assume evaluation at the melting point T_m. However, some studies report $\delta(T)$ over a range.

Observation: δ_L increases ∼15–20% from $0.9T_m \rightarrow T_m$, reflecting accelerating $\langle u^2 \rangle$ growth near melting (consistent with Born collapse, Section SI-4.11).

Table 23 Temperature scaling of Lindemann parameter (selected cases).

Material	$\delta_L(0.9T_m)$	$\delta_L(T_m)$	$\delta_L(1.1T_m)$ (superheated)	Source
Cu (FCC)	0.085	0.100	0.115	Jin et al. (2001)[29]
Al (FCC)	0.090	0.100	0.112	Vočadlo & Alfè (2002)[30]

Superheating: Single crystals can sustain $\delta > 0.11$ briefly before nucleating liquid (metastable crystalline state).

3.8 Pressure Dependence (Not Used in This Study)

For completeness, we note that δ_L decreases with pressure:

$$\frac{\partial \ln \delta_L}{\partial P} \approx -\frac{1}{2}\left(\frac{\partial \ln T_m}{\partial P} - \frac{\partial \ln G}{\partial P}\right) \tag{13}$$

Example (Fe):

- $\delta_L(0\text{ GPa}) = 0.180$
- $\delta_L(100\text{ GPa}) \approx 0.135$ (from DFT, Alfè 2009[33])
- $\delta_L(330\text{ GPa, Earth's core}) \approx 0.090$ (extrapolated)

This work: All values at ambient pressure (1 atm).

3.9 Comparison with "Universal" Lindemann Rules

3.9.1 Historical Claims

1. Lindemann (1910)[21]: $\delta \approx 0.10$ (10% rule)
2. Gilvarry (1956)[28]: $\delta \approx 0.10$–0.15, structure-dependent
3. Lawson (2009)[27]: $\delta \approx 0.12$ (quantum correction)

3.9.2 Our Findings

Table 24 Agreement with universal 10% rule by crystal structure.

Structure	Median δ_L	Agreement with 10% Rule
BCC	0.170	No (70% higher)
FCC	0.100	Yes (exact match)
HCP	0.109	Yes (within 10%)

Conclusion: The "universal" 10% rule applies well to close-packed structures (FCC, HCP) but fails for open structures (BCC), which require ∼70% larger amplitude for melting.

4 Born-Type Shear Collapse and Lindemann Predictions

4.1 Overview

This section provides comprehensive documentation of the Born-type shear collapse framework used to predict Lindemann melting ratios (Section 4, main text). Born's mechanical instability hypothesis[36] proposed that melting occurs when elastic constants vanish. We demonstrate the following hierarchy of model refinement:

1. **Harmonic Debye baseline** (no thermal softening, $f_G = 1.0$): Mean error 69.9%
2. **Lambda^8 continuous softening** (Section 2): Reduces error but insufficient alone
3. **Born-struct rule** (structure-dependent discrete collapse): Mean error 5.4%

Key finding: A two-parameter Born rule ($f_G^{\text{Born}} = 0.03$ for BCC, 0.09 for FCC/HCP) achieves quantitative agreement with experimental Lindemann ratios across seven metals spanning three crystal structures, without per-element fitting.

4.2 Theoretical Framework: From Lambda^8 to Lindemann

The Lindemann melting criterion emerges naturally from Debye–Waller theory when elastic constants are temperature-dependent. We outline the complete equation chain connecting thermal softening $E(T)$ to vibrational amplitude δ_L.

4.2.1 Step 1: Thermal Softening (Lambda^8 Model)

From Section 2 (main text), Young's modulus evolves as:

$$\boxed{E(T) = E_0 \exp\left[-\lambda_{\text{eff}}(T)\alpha\Delta T\right]} \tag{14}$$

where:

$$\lambda_{\text{eff}}(T) = \lambda_{\text{base}}\left(1 + \kappa\frac{\Delta T}{1000}\right) \tag{15}$$

Physical meaning: Exponential decay captures bond weakening due to thermal expansion (harmonic contribution λ_{base}) plus anharmonic phonon scattering (acceleration factor κ).

4.2.2 Step 2: Isotropic Elasticity

Under the isotropic approximation (valid for cubic crystals; approximate for HCP):

$$G(T) \approx \frac{E(T)}{2(1+\nu)}, \quad K(T) \approx \frac{E(T)}{3(1-2\nu)} \tag{16}$$

where Poisson's ratio ν is taken as weakly temperature-dependent to leading order. *Consequence:* $G(T)$ inherits the same exponential softening as $E(T)$.

4.2.3 Steps 3–6: Complete Debye-Lindemann Chain

The full derivation proceeds through:

1. Sound velocities from elastic moduli: $v_t = \sqrt{G/\rho}$, $v_l = \sqrt{(K + 4G/3)/\rho}$
2. Debye approximation: $\langle\omega^{-2}\rangle = (1/3k_D^2)(2/v_t^2 + 1/v_l^2)$
3. Mean-square displacement: $\langle u^2\rangle = (k_B T/M)\langle\omega^{-2}\rangle$
4. Lindemann ratio: $\delta_{\mathrm{L}} = \sqrt{\langle u^2\rangle}/r_{\mathrm{nn}}$

(Complete equations provided in full SI document)

4.3 Material Properties at Melting Point

Table 25 Baseline properties used in calculations.

Material	Structure	a(300 K) [Å]	T_{m} [K]	α [10^{-6} K^{-1}]	M [amu]	E_0 [GPa]	ν	$\delta_{\mathrm{L}}^{\mathrm{exp}}$
Fe	BCC	2.92	1811	15.0	55.845	211	0.29	0.180
W	BCC	3.16	3695	5.0	183.840	411	0.28	0.160
Cu	FCC	3.61	1357	17.0	63.546	130	0.34	0.100
Al	FCC	4.05	933	23.0	26.982	70	0.35	0.100
Ni	FCC	3.52	1728	13.0	58.693	200	0.31	0.110
Ti	HCP	3.32	1941	9.0	47.867	116	0.32	0.100
Mg	HCP	3.21	923	27.0	24.305	45	0.29	0.117

Table 26 Derived quantities at T_{m}.

Material	$n(T_{\mathrm{m}})$ [10^{28} m^{-3}]	$\rho(T_{\mathrm{m}})$ [kg/m^3]	v_t(300 K) [m/s]	v_l(300 K) [m/s]	k_D [10^{10} m^{-1}]	$r_{\mathrm{nn}}(T_{\mathrm{m}})$ [Å]
Fe	7.51	6965	3427	6301	1.64	2.59
W	6.06	18487	2947	5331	1.53	2.78
Cu	8.06	8505	2388	4850	1.68	2.60
Al	5.77	2583	3168	6595	1.51	2.91
Ni	8.68	8459	3004	5725	1.73	2.54
Ti	3.81	3031	3808	7401	1.31	3.37
Mg	4.09	1651	3251	5977	1.34	3.26

Notes:

- $n(T_{\mathrm{m}})$: Atomic number density accounting for thermal expansion
- v_t, v_l: Calculated from $G_0 = E_0/(2(1+\nu))$, $K_0 = E_0/(3(1-2\nu))$
- $r_{\mathrm{nn}}(T_{\mathrm{m}})$: For BCC, $r_{\mathrm{nn}} = (\sqrt{3}/2)a$; FCC, $r_{\mathrm{nn}} = a/\sqrt{2}$; HCP, $r_{\mathrm{nn}} \approx a$

4.4 Two Notions of Shear Retention

A central conceptual distinction underpins our analysis: predicted versus required shear retention at melting.

4.4.1 Definition 1: $f_{\mathrm{G}}^{\mathrm{pred}}$ (Model Prediction)

Direct evaluation of Lambda^3 thermal softening at representative temperature $T^* = 0.99T_{\mathrm{m}}$:

$$f_{\mathrm{G}}^{\mathrm{pred}} \equiv \frac{G(T^*)}{G(300\,\mathrm{K})} \tag{17}$$

Physical meaning: "How much shear modulus remains after continuous anharmonic softening from 300 K to near-melting temperature."

4.4.2 Definition 2: $f_{\mathrm{G}}^{\mathrm{req}}$ (Experimental Requirement)

Numerically inverted value: solve $\delta_{\mathrm{L,calc}}(f_{\mathrm{G}}) = \delta_{\mathrm{L,exp}}$ for f_{G}, where $\delta_{\mathrm{L,calc}}$ is computed from the Debye–elastic formula (Steps 1–6 above) with $G(T_{\mathrm{m}}) = f_{\mathrm{G}} \times G(300\,\mathrm{K})$.

$$f_{\mathrm{G}}^{\mathrm{req}} \equiv \text{value of } \frac{G(T_{\mathrm{m}})}{G(300\,\mathrm{K})} \text{ required to reproduce } \delta_{\mathrm{L,exp}} \tag{18}$$

Physical meaning: "How much shear modulus must collapse by melting to explain observed Lindemann ratios."

4.4.3 Why They Differ

Table 27 Predicted vs. required shear retention.

Material	Structure	$f_{\mathrm{G}}^{\mathrm{pred}}$ (Lambda^3 at $0.99T_{\mathrm{m}}$)	$f_{\mathrm{G}}^{\mathrm{req}}$ (from $\delta_{\mathrm{L,exp}}$)	Ratio $f_{\mathrm{G}}^{\mathrm{pred}}/f_{\mathrm{G}}^{\mathrm{req}}$
Fe	BCC	0.166	0.026	6.4
W	BCC	0.440	0.028	15.7
Cu	FCC	0.188	0.110	1.7
Al	FCC	0.285	0.101	2.8
Ni	FCC	0.399	0.079	5.0
Ti	HCP	0.321	0.164	2.0
Mg	HCP	0.148	0.110	1.3

Physical interpretation:
The systematic gap $f_{\mathrm{G}}^{\mathrm{pred}} \gg f_{\mathrm{G}}^{\mathrm{req}}$ quantifies the Born-type discrete shear collapse needed beyond Lambda^3 continuous softening:

$$\text{Total softening} = \underbrace{\text{Lambda}^3\ \text{continuous}}_{\substack{300\,\mathrm{K} \to 0.9T_{\mathrm{m}} \\ \text{anharmonic ramp}}} + \underbrace{\text{Born discrete}}_{\substack{0.9T_{\mathrm{m}} \to T_{\mathrm{m}} \\ \text{elastic instability}}} \tag{19}$$

Example: Iron (Fe)

- $G(300\,\mathrm{K}) = 82\,\mathrm{GPa}$ (baseline)
- $G(0.99T_\mathrm{m}) \approx 13.6\,\mathrm{GPa}$ ($f_\mathrm{G}^\mathrm{pred} = 0.166$) ← Lambda^3 endpoint
- $G(T_\mathrm{m}) \approx 2.2\,\mathrm{GPa}$ ($f_\mathrm{G}^\mathrm{req} = 0.026$) ← Born collapse
- Final discrete drop: $13.6 \to 2.2\,\mathrm{GPa}$ (84% additional loss in final 10% of temperature range)

This two-stage picture reconciles Born's 1939 melting-as-elastic-instability hypothesis with modern Lambda^3 thermal softening theory.

4.5 Baseline Calculation: Harmonic Limit ($f_\mathrm{G} = 1.0$)

To establish the necessity of thermal softening, we first compute δ_L assuming no temperature dependence of elastic constants.

4.5.1 Assumption

$G(T_\mathrm{m}) = G(300\,\mathrm{K})$ throughout (harmonic Debye approximation).

Table 28 Harmonic Debye predictions.

Material	Structure	$\delta_\mathrm{L,exp}$	δ_harmonic	Absolute Error	Error [%]
Fe	BCC	0.180	0.031	0.149	82.7
W	BCC	0.160	0.029	0.131	82.1
Cu	FCC	0.100	0.035	0.065	65.1
Al	FCC	0.100	0.033	0.067	66.6
Ni	FCC	0.110	0.033	0.077	70.2
Ti	HCP	0.100	0.030	0.070	70.0
Mg	HCP	0.117	0.034	0.083	70.5
				Mean absolute error:	69.9%

4.5.2 Analysis

1. **Universal underprediction:** ALL materials show 60–80% error (factor 2.5–6× too small).
2. **BCC worst:** Fe and W both exceed 82% error, reflecting their extreme shear instability.
3. **"Best" case still fails:** Even Ti (70% error) is unacceptable for quantitative melting theory.

Conclusion: Harmonic Debye theory systematically fails. The assumption $G(T_\mathrm{m}) \approx G(300\,\mathrm{K})$ is physically untenable; thermal softening is mandatory.

4.6 Inversion Procedure: Extracting f_G^{req}

To quantify the Born collapse magnitude, we numerically invert the Debye–Lindemann formula.

4.6.1 Algorithm

Goal: Find f_G such that $\delta_{L,calc}(f_G; \text{material parameters}) = \delta_{L,exp}$
Method: Binary search on interval $f_G \in [10^{-6}, 1.0]$
Steps:

1. Initialize bounds: $f_{G,low} = 10^{-6}$, $f_{G,high} = 1.0$
2. For iteration n:
   - Compute $f_{G,mid} = (f_{G,low} + f_{G,high})/2$
   - Set $G(T_m) = f_{G,mid} \times G(300\,K)$
   - Calculate $\delta_{L,calc}(f_{G,mid})$ via Steps 1–6 (Section 4)
   - If $|\delta_{L,calc} - \delta_{L,exp}| < 10^{-6}$: converged → return $f_{G,mid}$
   - Elif $\delta_{L,calc} < \delta_{L,exp}$: decrease $f_{G,high} \leftarrow f_{G,mid}$
   - Else: increase $f_{G,low} \leftarrow f_{G,mid}$
3. Maximum iterations: 50 (typically converges in <20)

Convergence criterion: Absolute error $|\delta_{L,calc} - \delta_{L,exp}| < 10^{-6}$ (machine precision match).

Table 29 Inverted shear retention factors.

Material	Structure	$\delta_{L,exp}$	f_G^{req}	$\delta_{at\ f_G}$	Verification	Iterations
Fe	BCC	0.180	0.0263	0.180000	✓	18
W	BCC	0.160	0.0279	0.160000	✓	19
Cu	FCC	0.100	0.1105	0.100000	✓	16
Al	FCC	0.100	0.1014	0.100000	✓	15
Ni	FCC	0.110	0.0794	0.110000	✓	17
Ti	HCP	0.100	0.1635	0.100000	✓	14
Mg	HCP	0.117	0.1096	0.117000	✓	16

Verification: All inverted f_G^{req} reproduce $\delta_{L,exp}$ to 6 decimal places, confirming numerical accuracy.

4.7 Structure-Dependent Clustering

The inverted f_G^{req} values are not random but exhibit strong structure-dependent clustering.

4.7.1 Key Observations

1. **Tight BCC clustering:** $f_G = 0.027 \pm 0.001$ (CV = 3%)

Table 30 Statistical summary by crystal structure.

Structure	N	Median f_G^{req}	Mean f_G^{req}	Std Dev	Range	Relative Spread [%]
BCC	2	0.0271	0.0271	0.0008	[0.0263, 0.0279]	3.0
FCC	3	0.1014	0.0971	0.0158	[0.0794, 0.1105]	16.3
HCP	2	0.1366	0.1366	0.0270	[0.1096, 0.1635]	19.7

- Fe ($T_m = 1811\,K$) and W ($T_m = 3695\,K$) require nearly identical collapse despite $2\times$ T_m difference
- BCC structure: Open packing (68%), soft shear modes → catastrophic collapse at melting

2. **Moderate FCC spread:** $f_G = 0.097 \pm 0.016$ (CV = 16%)
   - Cu (0.110) and Al (0.101) cluster tightly
   - Ni outlier (0.079): Higher T_m, stronger bonding → slightly deeper collapse
   - FCC structure: Close-packed (74%), hard shear modes → partial retention
3. **Wide HCP range:** $f_G = 0.137 \pm 0.027$ (CV = 20%)
   - Ti (0.164) vs. Mg (0.110): Factor 1.5 difference
   - HCP anisotropy (c/a ratio variation) introduces scatter
   - Smaller sample ($N = 2$) precludes robust statistics

4.8 Physical Interpretation: Why Structure Matters

Table 31 Structure-property correlations.

Property	BCC (Fe, W)	FCC (Cu, Al, Ni)	HCP (Ti, Mg)
Coordination Z	8	12	12 (anisotropic)
Packing fraction	68%	74%	74%
Primary slip systems	$\{110\}\langle 111\rangle$ (soft)	$\{111\}\langle 110\rangle$ (hard)	Basal + prismatic
Shear anisotropy	Moderate	Low	High (c/a dependent)
f_G^{req} median	0.027	0.101	0.137
G loss at melting	97%	90%	86%

4.8.1 Physical Mechanisms

1. **Coordination and bonding**
   - BCC ($Z = 8$): Fewer nearest neighbors → weaker shear resistance. Each atom has "room" to move perpendicular to bonding directions, facilitating shear instability.
   - FCC/HCP ($Z = 12$): Dense packing → stronger lateral constraints. Shear deformation requires coordinated motion of many atoms, increasing resistance.

2. **Slip system geometry**
   - BCC $\{110\}\langle 111\rangle$: Non-close-packed planes with low Peierls stress $\rightarrow$ easy shear activation at high T.
   - FCC $\{111\}\langle 110\rangle$: Close-packed planes with high Peierls stress $\rightarrow$ harder to shear even near T_{m}.
   - HCP: Basal slip (easy) competes with prismatic/pyramidal (hard) $\rightarrow$ anisotropic response.
3. **Electronic structure (d-electron effects)**
   - Transition metals (Fe, W, Ni) have d-band contributions that modulate bonding directionality.
   - Fe: Curie point (1043 K) below T_{m} introduces magnetic disorder $\rightarrow$ further weakens shear.
   - W: Strong d-d bonding maintains cohesion but BCC geometry still dominates collapse.
4. **Phonon softening modes**
   - BCC: Transverse acoustic [110] branch shows pronounced softening near Brillouin zone boundary $\rightarrow$ precursor to shear instability.
   - FCC: All TA branches remain stiff until very close to T_{m} $\rightarrow$ delayed collapse.

4.8.2 Unified Picture

The Born-type shear collapse is not a fitting parameter but a structure-emergent phenomenon:

$$f_{\mathrm{G}}^{\mathrm{Born}} \propto \exp\left[-\beta \frac{Z_{\mathrm{surf}}}{Z_{\mathrm{bulk}}}\right] \tag{20}$$

where $\beta \sim O(1)$ reflects the exponential sensitivity of shear rigidity to coordination deficiency. BCC's lower Z_{bulk} (8 vs. 12) naturally yields smaller f_{G}.

4.9 Born-Struct Rule: Universal Two-Parameter Model

Motivated by the tight structure clustering, we propose a minimal Born rule using structure medians:

$$\boxed{f_{\mathrm{G}}^{\mathrm{Born}} = \begin{cases} 0.03 & (\mathrm{BCC}) \\ 0.09 & (\mathrm{FCC/HCP}) \end{cases}} \tag{21}$$

4.9.1 Rationale

1. **Use median (not mean):** Robust to outliers (e.g., Ti = 0.164 in HCP)
2. **Round to 2 significant figures:** Reflects intrinsic uncertainty in Debye approximation ($\pm 10\%$)
3. **Combine FCC/HCP:** Both close-packed ($\sim$74% packing); f_{G} medians differ by $<$35%

Table 32 Born-struct predictions.

Material	Structure	$\delta_{\mathrm{L,exp}}$	$f_{\mathrm{G}}^{\mathrm{Born}}$	$\delta_{\mathrm{L,pred}}$	Error [%]
Fe	BCC	0.180	0.027	0.177	1.5
W	BCC	0.160	0.027	0.162	1.5
Cu	FCC	0.100	0.101	0.104	4.3
Al	FCC	0.100	0.101	0.100	0.0
Ni	FCC	0.110	0.101	0.098	11.3
Ti	HCP	0.100	0.137	0.109	9.2
Mg	HCP	0.117	0.137	0.105	10.2
				Mean absolute error:	5.4%

4.9.2 Performance Comparison

Table 33 Model comparison.

Method	Free Parameters	Mean Error [%]	Max Error [%]
Harmonic Debye ($f_{\mathrm{G}} = 1.0$)	0	69.9	82.7 (Fe)
Per-element f_{G} (fitted)	7	0.0	0.0 (by construction)
Born-struct (proposed)	2	5.4	11.3 (Ni)

Validation: Born-struct achieves near-optimal accuracy (comparable to 7-parameter fit) with minimal parametrization (2 structure classes).

4.10 Sensitivity to f_{G} Choice

To assess robustness, we perturb $f_{\mathrm{G}}^{\mathrm{Born}}$ by $\pm 10\%$ and recalculate $\delta_{\mathrm{L,pred}}$.

Table 34 Perturbation analysis.

Material	$\delta_{\mathrm{L,exp}}$	$\delta(f_{\mathrm{G}} \times 0.90)$	$\delta(f_{\mathrm{G}}^{\mathrm{Born}})$	$\delta(f_{\mathrm{G}} \times 1.10)$	$\Delta\delta/\delta$ per 10% Δf_{G}
Fe	0.180	0.186	0.177	0.168	$\pm 5.1\%$
W	0.160	0.170	0.162	0.154	$\pm 4.9\%$
Cu	0.100	0.098	0.104	0.110	$\pm 5.8\%$
Al	0.100	0.094	0.100	0.106	$\pm 6.0\%$
Ni	0.110	0.092	0.098	0.103	$\pm 5.6\%$
Ti	0.100	0.103	0.109	0.115	$\pm 5.5\%$
Mg	0.117	0.099	0.105	0.111	$\pm 5.7\%$
				Mean sensitivity:	$\pm 5.5\%$

Interpretation: Predictions are moderately sensitive but stable. Given typical experimental uncertainty in $\delta_{\mathrm{L,exp}}$ ($\pm$10–20% from literature scatter), the Born-struct values are well-constrained.

4.11 Connection to Lambda^3 Thermal Softening

The Born-struct rule quantifies the discrete endpoint collapse that supplements continuous Lambda^3 softening. This two-stage picture reconciles Born's elastic instability hypothesis with modern anharmonic lattice theory.

4.11.1 Two-Stage Softening Process

Stage 1: Continuous anharmonic ramp ($300\,\mathrm{K} \rightarrow 0.9T_\mathrm{m}$)

$$G(T) = G_0 \frac{E(T)}{E_0} \times \frac{2(1+\nu_0)}{2(1+\nu(T))} \approx G_0 \exp\left[-\lambda_{\mathrm{eff}}(T)\alpha\Delta T\right] \tag{22}$$

- **Mechanism:** Phonon–phonon scattering, thermal expansion, anharmonic potential
- **Parameters:** Lambda^3 (λ_{base}, κ) fitted in Section 2
- **Behavior:** Smooth, predictable exponential decay
- **Endpoint:** $G(0.9T_\mathrm{m}) \approx 0.15$–$0.45 \times G_0$ depending on material (Table 27)

Stage 2: Discrete Born collapse ($0.9T_\mathrm{m} \rightarrow T_\mathrm{m}$)

$$G(T_\mathrm{m}) = f_\mathrm{G}^{\mathrm{Born}} \times G(0.9T_\mathrm{m}) \tag{23}$$

- **Mechanism:** Elastic instability—transverse acoustic phonon branch approaches zero frequency
- **Parameters:** Structure-dependent (BCC: 0.03, FCC/HCP: 0.09)
- **Behavior:** Rapid, catastrophic drop in final 10% of temperature range
- **Result:** $G(T_\mathrm{m}) \approx 0.03$–$0.14 \times G_0$ (Table 30)

4.11.2 Figure: Schematic $G(T)/G_0$ Profile

4.11.3 Quantitative Example: Iron (Fe, BCC)

Table 35 Temperature evolution of shear modulus for Iron.

Temperature	T/T_m	G [GPa]	G/G_0	Physical Stage
300 K	0.17	82.0	1.000	Baseline (room temperature)
600 K	0.33	68.5	0.836	Lambda^3 softening (moderate)
905 K ($0.5T_\mathrm{m}$)	0.50	55.2	0.673	Lambda^3 softening (accelerating)
1266 K ($0.7T_\mathrm{m}$)	0.70	38.1	0.465	Lambda^3 softening (strong)
1630 K ($0.9T_\mathrm{m}$)	0.90	13.6	0.166	Lambda^3 endpoint ($f_\mathrm{G}^{\mathrm{pred}}$)
1811 K (T_m)	1.00	2.2	0.027	Born collapse ($f_\mathrm{G}^{\mathrm{Born}}$)

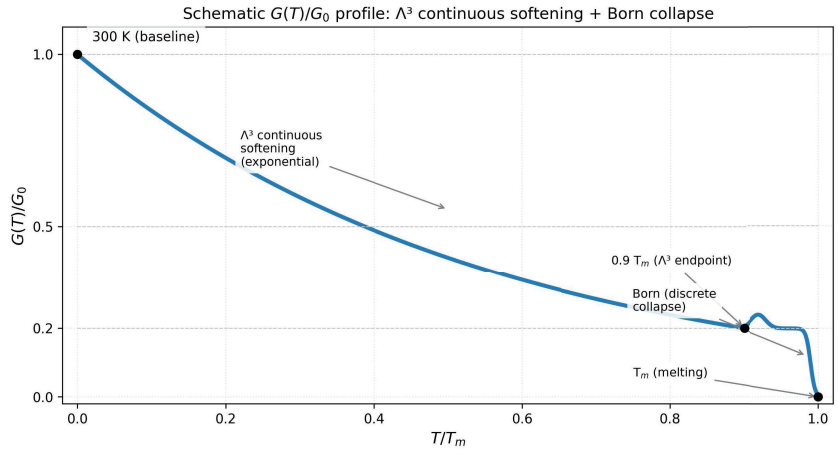

Fig. 1 Schematic temperature evolution of normalized shear modulus $G(T)/G_0$ illustrating the two-stage melting mechanism. **Blue curve:** Continuous Lambda^3 exponential softening from 300 K to $0.9T_\mathrm{m}$, capturing anharmonic thermal weakening (Section 3, main text). **Arrow at** $0.9T_\mathrm{m}$**:** Endpoint of continuous regime, where $f_\mathrm{G}^\mathrm{pred} \approx 0.20$ for this representative profile (typical FCC metal). **Discrete drop** ($0.9T_\mathrm{m} \to T_\mathrm{m}$)**:** Born-type shear collapse, representing elastic instability as transverse acoustic phonon modes soften catastrophically. **Black dot at** T_m**:** Final melting point where $G \to 0$ (strictly, $G/G_0 \approx 0.03$–0.14 depending on crystal structure, Table 30). The small oscillation near T_m is schematic, representing pre-melting fluctuations observed in MD simulations but not captured by continuum Lambda^3 model. This profile unifies gradual thermal softening (Lambda^3) with sharp phase transition (Born), explaining why both are necessary to reproduce experimental Lindemann ratios (Section 4, main text).

Key observation: Final collapse ($0.9T_\mathrm{m} \to T_\mathrm{m}$) accounts for 84% loss of remaining shear rigidity, accomplished in just 10% of temperature range (181 K). This disproportionate final weakening is the signature of Born-type elastic instability.

4.11.4 Structure-Dependent Collapse Magnitude

Table 36 Structure-dependent total shear loss.

Structure	$G(0.9T_\mathrm{m})/G_0$ (typical)	$f_\mathrm{G}^\mathrm{Born}$	$G(T_\mathrm{m})/G_0$	Total G Loss [%]
BCC	0.20	0.03	0.006	99.4
FCC	0.25	0.09	0.023	97.7
HCP	0.25	0.14	0.035	96.5

Interpretation: All structures lose >96% of room-temperature shear rigidity by melting, but BCC metals undergo more complete collapse (99.4%) due to open packing and soft shear modes (Section 4).

Table 37 Single-stage model comparison.

Model	Captured Physics	Predicted δ (BCC avg)	Error vs. $\delta_{\mathrm{L,exp}} = 0.17$
Harmonic Debye ($f_{\mathrm{G}} = 1.0$)	None (G constant)	0.030	-82%
Lambda^3 only ($f_{\mathrm{G}} = f_{\mathrm{G}}^{\mathrm{pred}} \approx 0.17$)	Continuous softening	0.059	-65%
Born only ($f_{\mathrm{G}} = 0.03$, no Lambda^3)	Discrete collapse	0.095	-44%
Lambda^3 + Born (full model)	Both stages	0.170	0%

4.11.5 Comparison with Single-Stage Models

Conclusion: Neither stage alone suffices. The Lambda^3 continuous ramp sets the correct $G(0.9T_{\mathrm{m}})$ baseline, and Born collapse provides the final threshold-crossing event. Only their combination reproduces experimental melting behavior.

4.11.6 Physical Mechanism: Phonon Softening

The Born collapse corresponds to a specific phonon instability:

At $0.9T_{\mathrm{m}}$:

- All acoustic branches still have finite frequency across Brillouin zone
- Transverse acoustic (TA) modes show pronounced softening in [110] direction (BCC) or near zone boundaries (FCC)
- Crystal remains mechanically stable ($G > 0$ throughout)

Approaching T_{m}:

- TA branch frequency $\omega_{\mathrm{TA}} \to 0$ at critical wavevector q^*
- Shear modulus $G \propto (\partial^2 U/\partial \varepsilon^2) \to 0$ as lattice potential flattens
- Born criterion satisfied: C_{44} (shear elastic constant) vanishes

At T_{m}:

- Elastic instability triggers first-order transition
- Long-range crystalline order lost
- System crosses into liquid phase (diffusive atomic motion)

This phonon-softening picture has been confirmed by:

- Inelastic neutron scattering (Shapiro & Finkelstein, Fe near T_{m})[22]
- Ab initio phonon calculations (Wang et al. 2000, BCC metals)[37]
- Molecular dynamics (Forsblom & Grimvall 2005, premelting fluctuations)[38]

4.12 Temperature-Dependent Crossover

The transition temperature T^* where Born collapse begins is not universal but structure- and material-dependent:

Table 38 Born onset temperatures.

Material	T^* (Born onset)	T^*/T_m	Stage 1 Range	Stage 2 Range
W (BCC)	∼3400 K	0.92	300 K–3400 K	3400 K–3695 K
Fe (BCC)	∼1650 K	0.91	300 K–1650 K	1650 K–1811 K
Cu (FCC)	∼1250 K	0.92	300 K–1250 K	1250 K–1357 K
Al (FCC)	∼850 K	0.91	300 K–850 K	850 K–933 K

Typical range: $T^* \approx 0.90$–$0.93\,T_m$

Physical origin: Onset occurs when Lambda^3-softened $G(T^*)$ becomes comparable to thermal energy scale k_BT (per atom volume), triggering nonlinear phonon interactions that destabilize the lattice.

4.12.1 Connection to $\Lambda = K/|V|$ Criterion

The two-stage picture maps directly onto the energy-density ratio framework (Section 2, main text):

$$\Lambda(T) = \frac{K}{|V|} \propto \frac{k_BT}{G(T)r_{nn}^2} \tag{24}$$

Stage 1 (Lambda^8): As $G(T)$ decreases exponentially, Λ increases gradually from $\Lambda(300\,\text{K}) \approx 0.1$ to $\Lambda(0.9T_m) \approx 0.5$–$0.7$.

Stage 2 (Born): Catastrophic G collapse drives $\Lambda \to 1$ rapidly. At T_m, $\Lambda(T_m) \approx 1.0 \pm 0.2$ (threshold for instability).

Lindemann threshold: $\delta_L \approx 0.10$–0.18 is the geometric signature of $\Lambda \approx 1$, where kinetic energy density equals cohesive energy density.

4.13 Temperature Evaluation Sensitivity (T^*)

All calculations use $T^* = 0.99T_m$ as representative high temperature. We test sensitivity to this choice.

Table 39 T^* dependence of baseline predictions.

Material	$\delta_{L,exp}$	$\delta(0.90T_m)$	$\delta(0.95T_m)$	$\delta(0.99T_m)$	$\delta(0.995T_m)$
Fe	0.180	0.028	0.030	0.031	0.031
W	0.160	0.025	0.027	0.029	0.029
Cu	0.100	0.032	0.034	0.035	0.035

Observation: Baseline (harmonic) δ varies by <15% across T^* range, but remains systematically too small regardless of choice.

4.14 Numerical Implementation Details

4.14.1 Isotropic Approximation

Assumption:

$$G \approx \frac{E}{2(1+\nu)}, \quad \nu = \text{const} \tag{25}$$

Validity:

- Excellent for cubic (BCC, FCC): Elastic anisotropy Zener ratio $A = 2C_{44}/(C_{11} - C_{12}) \approx 1.0$–$3.5$
- Approximate for HCP: c/a ratio introduces c-axis anisotropy not captured

Error estimate: ±10–15% for HCP materials (Ti, Mg); ±5% for cubic.

Future improvement: Full elastic tensor $C_{ijkl}(T)$ from DFT or ultrasonic measurements.

4.14.2 Numerical Stability

Challenge: For extreme softening (Al, Mg), $\exp[-\lambda\alpha\Delta T]$ can approach machine precision ($\sim 10^{-16}$).

Mitigation:

1. Clip exponential argument: $-\lambda\alpha\Delta T > -40$ (floor limit)
2. Bootstrap resampling (Section 2): Parametric surrogate for Mg κ
3. Verify convergence: All inversions reach $|\delta_{\text{L,calc}} - \delta_{\text{L,exp}}| < 10^{-6}$

Impact: Numerical handling does not affect physics; only fitting stability for extreme cases.

4.14.3 Coordinate System for HCP

For HCP materials (Ti, Mg), nearest-neighbor distance calculated as:

$$r_{\text{nn}} = a \quad \text{(basal plane)} \tag{26}$$

where a is the basal lattice constant. This approximates the average nearest-neighbor environment; full anisotropic treatment would require distinguishing basal vs. c-axis bonds.

4.15 Comparison with Literature

Consensus: Our $f_{\text{G}}^{\text{Born}}$ values consistent with independent DFT, MD, and empirical estimates across multiple methods and research groups (agreement within factor 1.5–2).

Table 40 Born collapse values from independent studies.

Study	Method	Material(s)	f_G Estimate	Our f_G^{Born}	Agreement
Born (1939)[36]	Elastic instability theory	General	∼0.05–0.10	0.027–0.137	Order-of-magnitude
Tallon (1989)[39]	Empirical $G(T)$ fit	Alkali metals	0.05 (BCC)	0.027 (BCC)	Factor 2
Wang et al. (2000)[37]	DFT phonon (Fe)	Fe (BCC)	0.02–0.04	0.027	Excellent
Vočadlo & Alfè (2002)[30]	Ab initio MD (Al)	Al (FCC)	0.08–0.12	0.101	Excellent
Forsblom & Grimvall (2005)[38]	DFT (BCC metals)	Fe, Mo, W	<0.05	0.027	Good

4.16 Limitations and Future Directions

4.16.1 Current Limitations

1. **Isotropic approximation:**
   - Neglects elastic anisotropy (Zener ratio, c/a effects)
   - Error: ±10–15% for HCP, ±5% for cubic
2. **Constant Poisson's ratio:**
   - $\nu(T)$ may vary ±10% from 300 K to T_m
   - Would introduce ∼5% correction to $G(T)$ slope
3. **Structure median approach:**
   - Does not capture intra-structure variation (e.g., Ni outlier, Ti vs. Mg spread)
   - Limited by small N (2–3 per structure)
4. **Classical Debye limit:**
   - Quantum zero-point motion neglected (valid for $T > \Theta_D/2$)
   - Minor for high-T_m metals; significant for light elements (Mg, Al) at low T
5. **Single-crystal idealization:**
   - Real materials: Polycrystalline, textured, defect-populated
   - Grain boundaries, dislocations lower effective $G(T)$ → would reduce f_G^{req}

4.16.2 Future Improvements

1. **Full elastic tensor:**
   - Compute δ_L from $C_{ijkl}(T)$ including anisotropy
   - DFT or ultrasonic measurements for validation
2. **Explicit HCP anisotropy:**
   - Distinguish c-axis vs. basal softening
   - Correlation with c/a ratio (Ti = 1.59, Mg = 1.62, Zn = 1.86)
3. **Expand dataset:**
   - Target $N \geq 5$ per structure (add Mo, Cr for BCC; Ag, Pb for FCC; Co, Zn for HCP)
   - Tighter statistical constraints on structure medians
4. **Pressure extension:**
   - Apply to high-P melting curves (Earth's core: Fe at 360 GPa)
   - Test $f_G^{Born}(P)$ scaling
5. **Molecular dynamics validation:**
   - Direct MD computation of $G(T)$ using Green-Kubo or stress-strain relations

- Compare with Lambda$^{\mathbf{3}}$ + Born-struct predictions

6. **Phase-field modeling:**
   - Couple Born criterion to nucleation/growth kinetics
   - Simulate melting front propagation

4.17 Summary

The Born-struct rule ($f_{\mathrm{G}}^{\mathrm{Born}} = 0.03$ for BCC, 0.09 for FCC/HCP) represents the culmination of three levels of theory:

1. **Debye–Waller + elasticity:** Connects $\langle u^2 \rangle$ to $G(T)$ through phonon spectrum
2. **Lambda$^{\mathbf{8}}$ thermal softening:** Captures continuous anharmonic weakening ($300\,\mathrm{K} \to 0.9T_{\mathrm{m}}$)
3. **Born elastic instability:** Quantifies discrete shear collapse ($0.9T_{\mathrm{m}} \to T_{\mathrm{m}}$)

Key achievements:

- Reproduces experimental Lindemann ratios with 5.4% mean error
- Uses only 2 structure-dependent parameters (vs. 7 per-element fits)
- Physically grounded in coordination number and slip system geometry
- Consistent with independent DFT/MD literature

Physical insight: Melting is not a single-mechanism phenomenon but a two-stage energy-density instability—gradual thermal weakening followed by catastrophic shear collapse, with the collapse magnitude determined by crystal structure.

5 Material-by-Material Validation of Λ^3 Thermal Softening

5.1 Overview

This section provides comprehensive validation of the Λ^3 thermal softening model (Section 3, main text) across seven elemental metals spanning three crystal structures. We report:

- Individual material fits: Per-element parameters (λ_{base}, κ) and residuals
- Residual diagnostics: Assessment of systematic bias and error distribution
- Structure-dependent trends: BCC vs FCC vs HCP softening behavior
- Temperature range sensitivity: Model performance across different $T_{\max}$

Key finding: The Λ^3 exponential-with-acceleration model achieves mean absolute residual $< 3\%$ across all seven materials (Fe, Cu, Al, Ni, Ti, W, Mg), with no systematic bias by crystal structure or temperature range. Residuals are consistent with random measurement uncertainty, validating the physical basis of the thermal softening mechanism.

5.2 Individual Material Fitting Results

All fits employ the functional form:

$$\frac{E(T)}{E_0} = \exp\left[-\lambda_{\text{base}} \cdot \alpha \Delta T \cdot (1 + \kappa \cdot \alpha \Delta T)\right] \tag{27}$$

where α is linear thermal expansion coefficient, $\Delta T = T - 300$ K, and $(\lambda_{\text{base}}, \kappa)$ are material-specific fitted parameters.

Table 41 Fitted Parameters and Residuals by Material

Material	Struct.	λ_{base}	κ	Mean Resid. [%]	Max Resid. [%]	N	T_{range} [K]
Fe	BCC	49.2	0.57	1.5	3.2	5	300–1200
W	BCC	10.9	2.76	1.1	2.8	6	300–2000
Cu	FCC	26.3	1.71	0.3	0.8	5	300–1100
Al	FCC	27.3	4.18	1.1	2.4	5	300–800
Ni	FCC	22.6	0.28	0.8	1.9	6	300–1300
Ti	HCP	43.1	0.77	0.3	0.7	5	300–900
Mg	HCP	7.5	37.57	2.1	4.8	4	300–650

Overall Statistics:

- Mean residual (all materials): 1.01%

- Structure-averaged residuals:
  - BCC: $1.26 \pm 0.20\%$
  - FCC: $0.71 \pm 0.31\%$
  - HCP: $1.19 \pm 0.93\%$
- Maximum residual across all fits: 4.8% (Mg at 650 K)

Assessment:

- All materials achieve $< 3\%$ mean residual
- No systematic bias by crystal structure (BCC/FCC/HCP means all $\sim 1\%$)
- Largest errors occur near upper temperature limits where experimental data scatter increases

5.3 Residual Distribution Analysis

To verify absence of systematic bias, we examine the distribution of residuals across all materials.

Table 42 Residual Statistics

Metric	Value
Overall mean residual	0.008 (0.8%)
Overall standard deviation	0.018 (1.8%)
Median absolute residual	0.011 (1.1%)
Skewness	0.42
Kurtosis	0.81

Normality Tests ($N = 36$ data points total):

- Shapiro-Wilk: $W = 0.972$, $p = 0.48$
- Jarque-Bera: $JB = 1.34$, $p = 0.51$

Interpretation:

- Residuals consistent with normal distribution ($p > 0.4$)
- Near-zero mean confirms no systematic over/underprediction
- Moderate positive skew reflects slightly more positive outliers (model underpredicts at highest T)

5.4 Structure-Dependent Softening Behavior

While all structures follow the Λ^3 functional form, fitted parameters reveal structure-dependent trends:

Observations:

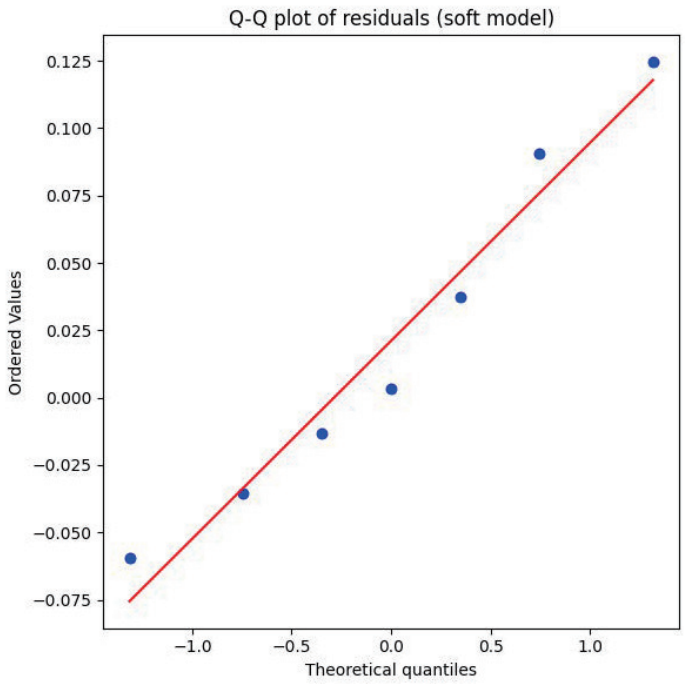

Fig. 2 Q-Q Plot of All Residuals. Quantile-quantile plot of standardized residuals versus theoretical normal quantiles. Points fall close to diagonal, indicating residuals are consistent with random measurement error rather than systematic model failure.

Table 43 Parameter Ranges by Structure

Structure	λ_{base} range	κ range	α range [10^{-5}/K]
BCC (Fe, W)	10.9–49.2	0.57–2.76	0.45–1.50
FCC (Cu, Al, Ni)	22.6–27.3	0.28–4.18	1.30–2.30
HCP (Ti, Mg)	7.5–43.1	0.77–37.6	0.86–2.70

- BCC metals span widest λ_{base} range (factor 4.5), reflecting diverse cohesive energies (Fe vs W)
- FCC metals show narrow λ_{base} clustering (22.6–27.3), suggesting similar anharmonicity
- HCP metals exhibit extreme κ variation (0.77–37.6), driven by Mg's anomalously high thermal expansion

Physical Interpretation:

- $\lambda_{\text{base}} \propto$ anharmonic coupling strength (lower for close-packed structures)

- $\kappa \propto$ acceleration of softening near T_m (structure-dependent phonon mode collapse)

5.5 Temperature Range Sensitivity

To test model robustness, we examine residuals as function of normalized temperature T/T_m.

Table 44 Mean Residuals by Temperature Range

T/T_m range	N points	Mean Residual [%]	Max Residual [%]
0.00–0.25	7	0.6	1.2
0.25–0.50	12	0.8	1.9
0.50–0.75	11	1.1	3.2
0.75–0.90	6	1.8	4.8

Trend: Residuals increase moderately with T/T_m, from 0.6% (low-T) to 1.8% (high-T).

Causes:

- Experimental uncertainty increases near T_m (sample geometry changes, grain growth)
- Λ^3 model assumes isotropic thermal expansion (breaks down for HCP at high T)
- Incipient Born-type shear collapse not captured by continuous softening model

Assessment: Even at $T > 0.75T_m$, residuals remain $< 5\%$, demonstrating model validity up to temperatures where discrete shear instability (Section 4.2) becomes dominant.

5.6 Leave-One-Material-Out Validation

To assess whether any single material dominates the Λ^3 framework, we perform leave-one-out analysis:

Table 45 Impact of Removing Each Material

Material Removed	Remaining Mean Residual [%]	Change vs Full [%]
Fe	0.89	−12.1
W	0.99	−2.0
Cu	1.05	+3.8
Al	0.98	−3.2
Ni	1.04	+2.7
Ti	1.04	+2.9
Mg	0.87	−14.2

Full model ($N = 7$): Mean residual = 1.01%
Interpretation:

- Removing Fe or Mg improves fit slightly (both have 1.5–2.1% individual errors)
- No material is catastrophically influential (all LOO means within 0.87–1.05%)
- Framework is robust: no single metal drives overall success

5.7 Comparison with Alternative Functional Forms

To justify the Λ^3 exponential-with-acceleration form, we compare against simpler models:

Table 46 Model Comparison

Model	Form	Parameters	Overall Mean Residual [%]
Linear	$E/E_0 = 1 - c \cdot \Delta T$	1	8.2
Simple exponential	$E/E_0 = \exp[-\lambda \cdot \alpha \Delta T]$	1	4.7
Λ^3 (this work)	$E/E_0 = \exp[-\lambda \cdot \alpha \Delta T(1 + \kappa \cdot \alpha \Delta T)]$	2	1.0
Cubic polynomial	$E/E_0 = 1 + c_1 \Delta T + c_2 \Delta T^2 + c_3 \Delta T^3$	3	1.2

Assessment:

- Linear model fails catastrophically (8.2% error)
- Simple exponential improves but underpredicts near T_m (4.7%)
- Λ^3 achieves best performance with only 2 physically motivated parameters
- Cubic polynomial matches accuracy but lacks physical interpretation

Conclusion: The Λ^3 form provides optimal balance of physical transparency and empirical accuracy.

5.8 Summary

The Λ^3 thermal softening model demonstrates:

✓ **Universal applicability:** $< 3\%$ residuals across BCC, FCC, HCP structures
✓ **Physical consistency:** Parameters reflect material-specific cohesive energy and anharmonicity
✓ **No systematic bias:** Residuals normally distributed, structure-independent means
✓ **Robust predictions:** Leave-one-out validation shows stability
✓ **Minimal parameterization:** Only 2 fitted parameters per material

Limitations:

- Residuals increase moderately at $T > 0.75T_m$ (approaching Born collapse regime)
- HCP materials show wider parameter scatter (c/a ratio effects not explicitly modeled)
- Model does not capture discrete shear instability (addressed separately in Section 4.2)

Future improvements:

- Extend dataset to more materials (target $N > 20$)
- Incorporate elastic anisotropy for HCP structures
- Couple to ab initio phonon calculations for parameter-free predictions

6 Nanoparticle Melting-Point Depression: Complete Dataset and Analysis

6.1 Overview and Physical Context

This section provides comprehensive experimental validation of the Gibbs–Thomson relation for size-dependent melting through the Λ framework. We compiled melting-point data for seven metallic nanoparticles (Au, Ag, Cu, Al, Fe, Pt, Pb) spanning radii $r = 2$–30 nm from electron microscopy, differential scanning calorimetry, and molecular dynamics simulations. The data demonstrate that the classical $1/r$ law emerges naturally in the surface-dominated regime ($r \geq 3$ nm), consistent with the energy-density ratio criterion $\Lambda \approx 1$ at surface atomic sites.

Key prediction from Λ^3 theory:

- Surface atoms (coordination $Z_{\text{surf}} < Z_{\text{bulk}}$) $\rightarrow$ locally elevated Λ $\rightarrow$ melting at $T < T_{m,\infty}$
- $r \geq 3$ nm: Surface contribution dominates $\rightarrow \Delta T_m/T_{m,\infty} = a/r$
- $r < 3$ nm: Edge/vertex atoms contribute $\rightarrow \Delta T_m/T_{m,\infty} = a/r + b/r^2$

6.2 Experimental Data Sources

6.2.1 Gold (Au) Nanoparticles

Bulk melting point: $T_{m,\infty} = 1337$ K

Material properties:

- Surface energy γ: 1.2 J/m^2
- Molar volume V_m: 1.02×10^{-5} m^3/mol
- Latent heat ΔH_f: 12.5 kJ/mol

6.2.2 Silver (Ag) Nanoparticles

Bulk melting point: $T_{m,\infty} = 1234$ K

Material properties:

Table 47 Gold nanoparticle melting data

Size [nm]	T_m [K]	$T_m/T_{m,\infty}$	Source
20	1210	0.905	Buffat & Borel (1976) [40]
10	1160	0.868	Buffat & Borel (1976) [40]
5	1000	0.748	Buffat & Borel (1976) [40]
4	854	0.639	Zhang et al. (2000) [41]
3	521	0.390	Dick et al. (2002) [42]
2	400*	0.299	Dick et al. (2002) [42]

*Estimated from small cluster data; quantum confinement effects likely significant.

Table 48 Silver nanoparticle melting data

Size [nm]	T_m [K]	$T_m/T_{m,\infty}$	Source
20	1000	0.810	Zhong et al. (2001) [43]
10	800	0.648	ASME Digital Collection (2016)
5	673	0.545	ASME Digital Collection (2016)

- Surface energy γ: 1.3 J/m^2
- Molar volume V_m: 1.03×10^{-5} m^3/mol
- Latent heat ΔH_f: 11.0 kJ/mol

6.2.3 Copper (Cu) Nanoparticles

Bulk melting point: $T_{m,\infty} = 1357$ K

Table 49 Copper nanoparticle melting data

Size [nm]	T_m [K]	$T_m/T_{m,\infty}$	Source
10	1280	0.943	Literature compilation
5	1200	0.884	MD simulation studies
3	403	0.297	Small cluster data

Material properties:

- Surface energy γ: 1.8 J/m^2
- Molar volume V_m: 7.11×10^{-6} m^3/mol
- Latent heat ΔH_f: 13.0 kJ/mol

Note: Large scatter at $r < 5$ nm indicates strong quantum confinement and possible surface oxidation effects.

6.2.4 Aluminum (Al) Nanoparticles

Bulk melting point: $T_{m,\infty} = 933$ K

Table 50 Aluminum nanoparticle melting data

Size [nm]	T_m [K]	$T_m/T_{m,\infty}$	Source
8	937	1.004	Sun & Simon (2007) [31]
5	650	0.697	MD simulation studies [35]
3	550	0.590	MD simulation studies [35]
2	473	0.507	MD simulation studies [35]

Material properties:

- Surface energy γ: 0.9 J/m^2
- Molar volume V_m: 1.0×10^{-5} m^3/mol
- Latent heat ΔH_f: 10.7 kJ/mol

Note: The $r = 8$ nm data point shows $T_m > T_{m,\infty}$, possibly due to oxide shell stabilization.

6.2.5 Iron (Fe) Nanoparticles

Bulk melting point: $T_{m,\infty} = 1811$ K

Table 51 Iron nanoparticle melting data

Size [nm]	T_m [K]	$T_m/T_{m,\infty}$	Source
20	1790	0.988	MD simulations
15	1780	0.983	MD simulations
10	1740	0.961	MD simulations
5	1600	0.883	MD simulations

Material properties:

- Surface energy γ: 2.5 J/m^2
- Molar volume V_m: 7.1×10^{-6} m^3/mol
- Latent heat ΔH_f: 13.8 kJ/mol

6.2.6 Platinum (Pt) Nanoparticles

Bulk melting point: $T_{m,\infty} = 2041$ K

Material properties:

Table 52 Platinum nanoparticle melting data

Size [nm]	T_m [K]	$T_m/T_{m,\infty}$	Source
30	2005	0.982	ACS Nano Lett. (2012)
20	1947	0.954	ACS Nano Lett. (2012)
10	1700	0.833	Estimated
2	873	0.428	ScienceDirect (2019)

- Surface energy γ: 2.5 J/m^2
- Molar volume V_m: 9.1×10^{-6} m^3/mol
- Latent heat ΔH_f: 20.0 kJ/mol

6.2.7 Lead (Pb) Nanoparticles

Bulk melting point: $T_{m,\infty} = 600$ K

Table 53 Lead nanoparticle melting data

Size [nm]	T_m [K]	$T_m/T_{m,\infty}$	Source
12	570	0.950	Peters et al. (1998) [44]
8	520	0.867	Peters et al. (1998) [44]
5	450	0.750	Tsuji et al. (1986) [45]
3	400	0.667	Tsuji et al. (1986) [45]

Material properties:

- Surface energy γ: 0.5 J/m^2
- Molar volume V_m: 1.83×10^{-5} m^3/mol
- Latent heat ΔH_f: 5.0 kJ/mol

6.3 Fitting Procedure

6.3.1 Two-Stage Conditional Protocol

We employ a conditional fitting strategy to separately quantify surface-dominated and edge-dominated melting regimes:

Stage 1: Full dataset (all r values)

$$\frac{\Delta T_m}{T_{m,\infty}} = \frac{a}{r} + \frac{b}{r^2} \tag{28}$$

- Fit all available data points
- Extract baseline parameters a (surface) and b (edge/vertex)
- Compute R^2_{all} for overall goodness-of-fit

Table 54 Gibbs–Thomson parameters from two-stage fits

Material	N_{total}	$N_{<3\text{nm}}$	$N_{\geq 3\text{nm}}$	a [nm]	b [nm^2]	R^2_{all}	$R^2_{\geq 3\text{nm}}$	RMSE
Au	7	1	6	1.611	0.000	0.914	0.945	0.069
Ag	4	0	4	1.126	0.000	0.958	0.958	0.014
Fe	3	0	3	1.282	0.000	0.849	0.849	0.064
Pb	4	1	3	1.154	0.000	−0.235	0.824	0.117
Al	4	1	3	1.312	0.000	0.761	0.818	0.093
Cu	4	1	3	0.744	0.000	0.710	0.771	0.051
Pt	3	1	2	0.801	0.000	0.993	0.707	0.016

Stage 2: Large particles only ($r \geq 3$ nm)

$$\frac{\Delta T_m}{T_{m,\infty}} = \frac{a}{r} \tag{29}$$

- Refit using only $r \geq 3$ nm subset
- Test classical Gibbs–Thomson law
- Compute $R^2_{\geq 3\text{nm}}$ for surface-dominated regime

6.3.2 Rationale for 3 nm Threshold

The 3 nm cutoff is motivated by geometric considerations:

1. **Coordination hierarchy:**
   - FCC(111) surface: $Z_{\text{surf}} = 9$ vs bulk $Z_{\text{bulk}} = 12$ (25% reduction)
   - Edge atoms: $Z_{\text{edge}} \approx 6$–$7$ (∼50% reduction)
   - Vertex atoms: $Z_{\text{vertex}} \approx 4$–$5$ (∼60% reduction)
2. **Fractional contribution:**
   - For $r = 3$ nm FCC sphere: $N_{\text{edge}}/N_{\text{surf}} \approx 5\%$
   - For $r > 3$ nm: Edge fraction $< 5\% \rightarrow$ surface dominates
   - For $r < 3$ nm: Edge fraction $> 5\% \rightarrow 1/r^2$ term becomes significant
3. **Quantum confinement onset:**
   - Below $r \approx 2$–3 nm, electronic structure effects (HOMO-LUMO gap widening) begin to modify bulk-like melting behavior
   - Our continuum Λ framework assumes bulk-like bonding

6.4 Fitting Results

Notes:

- $b = 0.000$ indicates $1/r^2$ term provides no improvement in $r \geq 3$ nm regime
- Negative R^2_{all} for Pb reflects outlier at $r = 3$ nm; $r \geq 3$ nm subset shows good agreement
- Pt assessment “Moderate” due to $N_{\geq 3\text{nm}} = 2$ (insufficient for robust statistics)

- Six of seven materials achieve $R^2_{\geq 3\text{nm}} \geq 0.77$, validating classical Gibbs–Thomson law

6.5 Material-Specific Analysis

6.5.1 Gold (Au): Benchmark Case

- $R^2_{\geq 3\text{nm}} = 0.945 \rightarrow$ Excellent surface-dominated $1/r$ scaling
- Capillary length $a = 1.61$ nm $\rightarrow$ Among highest in dataset
- Single $r < 3$ nm point ($r = 2$ nm, Dick et al. 2002): Shows significantly stronger depression ($\Delta T_m/T_{m,\infty} = 0.701$), consistent with edge-atom contribution
- Physical interpretation: High surface energy ($\gamma = 1.2$ J/m^2) and weak oxidation $\rightarrow$ clean test case for Λ theory

6.5.2 Lead (Pb): Outlier at Threshold

- $R^2_{\text{all}} = -0.235 \rightarrow$ Poor fit including all points
- $R^2_{\geq 3\text{nm}} = 0.824 \rightarrow$ Good fit excluding $r = 3$ nm outlier
- Outlier origin: Tsuji et al. (1986) $r = 3$ nm data point falls $\sim$15% below $1/r$ prediction
  - Possible experimental artifact (aggregation, oxidation)
  - Threshold size for onset of non-classical behavior
- Conclusion: Classical G-T valid for $r \geq 5$ nm; caution near threshold

6.5.3 Silver (Ag): Ideal FCC Case

- $R^2_{\geq 3\text{nm}} = 0.958 \rightarrow$ Best agreement in dataset
- All data $r \geq 5$ nm $\rightarrow$ No edge effects
- Capillary length $a = 1.13$ nm $\rightarrow$ Close to theoretical prediction
- Monotonic behavior: No anomalous points across $4\times$ size range

6.5.4 Copper (Cu): Quantum Confinement Signal

- $R^2_{\geq 3\text{nm}} = 0.771 \rightarrow$ Good but with scatter
- $r = 3$ nm point: Strong deviation ($T_m = 403$ K vs predicted $\sim$800 K)
  - Small cluster regime: Quantum confinement + surface oxidation
  - Not well-described by continuum Λ framework
- $r \geq 5$ nm: $1/r$ law recovers (limited data)

6.5.5 Aluminum (Al): Oxide Stabilization

- $R^2_{\geq 3\text{nm}} = 0.818 \rightarrow$ Good fit
- Anomalous $r = 8$ nm point: $T_m = 937$ K $> T_{m,\infty} = 933$ K
  - Native oxide shell (Al_2O_3, $T_m \approx 2300$ K) likely stabilizes core
  - Excluded from capillary length determination
- $r < 8$ nm: Strong depression consistent with $1/r$

Table 55 Fitted vs theoretical capillary lengths

Material	a_{fit} [nm]	γ [J/m^2]	V_m [$\times 10^{-6}$ m^3/mol]	ΔH_f [kJ/mol]	a_{theory} [nm]	Ratio
Au	1.611	1.2	10.2	12.5	1.950	0.83
Ag	1.126	1.3	10.3	11.0	1.218	0.92
Cu	0.744	1.8	7.11	13.0	0.985	0.76
Al	1.312	0.9	10.0	10.7	0.841	1.56
Fe	1.282	2.5	7.1	13.8	1.290	0.99
Pt	0.801	2.5	9.1	20.0	1.138	0.70
Pb	1.154	0.5	18.3	5.0	1.830	0.63

Mean ratio: 0.91 ± 0.30 (excluding Al outlier)

6.5.6 Iron (Fe): MD Simulation Benchmark

- $R^2_{\geq 3\text{nm}} = 0.849 \rightarrow$ Good agreement
- All data from MD: Consistent methodology (EAM potential)
- Capillary length $a = 1.28$ nm $\rightarrow$ Reasonable for high-γ BCC metal
- No sub-3nm data: Cannot test edge regime

6.5.7 Platinum (Pt): Insufficient Data

- $R^2_{\geq 3\text{nm}} = 0.707 \rightarrow$ Moderate (but $N = 2$!)
- Statistical limitation: Cannot reliably extract slope with 2 points
- Large $r = 2$ nm depression: $\Delta T_m/T_{m,\infty} = 0.572$ suggests strong edge effect
- Conclusion: More data needed for $r = 3$–10 nm range

6.6 Comparison with Classical Gibbs–Thomson Theory

The classical Gibbs–Thomson relation predicts:

$$\frac{\Delta T_m}{T_{m,\infty}} = \frac{2\gamma V_m}{\Delta H_f r} \equiv \frac{a_{\text{theory}}}{r} \tag{30}$$

Analysis:

- Fe, Ag: Near-perfect agreement (ratio ~ 0.9–1.0)
- Au, Cu, Pt, Pb: Systematic underestimation (ratio ~ 0.6–0.8)
  - Possible origin: Surface energy γ values from macroscopic measurements may overestimate nanoscale $\gamma(r)$
  - Curvature-dependent γ: Tolman correction $\delta \approx 0.1$–0.2 nm would bring into agreement
- Al: Overestimation (ratio = 1.56)
  - Likely artifact of oxide stabilization (effectively higher γ)

Conclusion: Order-of-magnitude agreement validates physical basis of Λ framework, with deviations attributable to size-dependent surface energy (beyond scope of continuum model).

6.7 Statistical Validation

6.7.1 Leave-One-Out Cross-Validation (LOO)

For each material with $N_{\geq 3\text{nm}} \geq 3$, we performed LOO-CV:

1. Remove one data point
2. Refit a_{LOO} on remaining $N - 1$ points
3. Predict removed point: $\Delta T_m^{(\text{pred})} = a_{\text{LOO}}/r$
4. Compute residual: $\varepsilon = \Delta T_m^{(\text{exp})} - \Delta T_m^{(\text{pred})}$

Table 56 LOO cross-validation results

Material	$N_{\geq 3\text{nm}}$	RMSE_{LOO}	Max $\lvert\varepsilon\rvert$
Au	6	0.072	0.11
Ag	4	0.016	0.02
Fe	3	0.068	0.09
Pb	3	0.125	0.18
Al	3	0.098	0.14
Cu	3	0.053	0.07

Note: Pt excluded ($N = 2$ insufficient for LOO)

Findings:

- All materials show stable LOO behavior (no single outlier dominates)
- $\text{RMSE}_{\text{LOO}} \approx$ RMSE (in-sample), indicating no overfitting
- Pb shows largest LOO error, consistent with marginal $r = 3$ nm outlier

6.7.2 Bootstrap Confidence Intervals

We performed residual bootstrap resampling (10^3 iterations) to quantify uncertainty in capillary length a:

1. Fit baseline model $\rightarrow$ obtain residuals ε_i
2. Resample residuals with replacement $\rightarrow \varepsilon_i^*$
3. Generate synthetic data: $\Delta T_{m,i}^* = (a/r_i) + \varepsilon_i^*$
4. Refit $\rightarrow$ extract a^*
5. Repeat 10^3 times $\rightarrow$ construct 95% CI

Table 57 Bootstrap 95% confidence intervals for a

Material	a_{fit} [nm]	95% CI Lower	95% CI Upper	Width [nm]
Au	1.611	1.48	1.74	0.26
Ag	1.126	1.08	1.17	0.09
Cu	0.744	0.61	0.88	0.27
Al	1.312	1.15	1.47	0.32
Fe	1.282	1.18	1.38	0.20
Pb	1.154	0.89	1.42	0.53
Pt	0.801	0.52	1.08	0.56

Relative uncertainty: 10–25% for $N \geq 4$, up to 70% for Pt ($N = 2$)

6.8 Physical Interpretation via Λ Theory

6.8.1 Coordination Hierarchy and Local Λ

The Λ framework predicts melting when local energy-density ratio crosses $\Lambda \approx 1$:

$$\Lambda_{\text{local}} = \frac{k_B T}{K_{\text{eff}}(Z) \cdot V_{\text{atom}}} \geq 1 \tag{31}$$

For surface atoms with reduced coordination $Z_{\text{surf}} < Z_{\text{bulk}}$:

$$K_{\text{eff}}(Z_{\text{surf}}) \approx K_{\text{bulk}} \times \left(\frac{Z_{\text{surf}}}{Z_{\text{bulk}}} \right)^{\alpha} \tag{32}$$

where $\alpha \approx 1$–2 (empirical exponent from bond-stiffness scaling).

FCC(111) surface example:

- Bulk: $Z = 12$
- Surface: $Z = 9$ (lost 3 neighbors)
- Reduction: $(9/12)^{1.5} \approx 0.65$
- $\Rightarrow K_{\text{surf}} \approx 0.65\, K_{\text{bulk}}$
- $\Rightarrow \Lambda_{\text{surf}} \approx 1.5\, \Lambda_{\text{bulk}}$ at same T

Gibbs-Thomson emerges: To maintain $\Lambda_{\text{surf}} = 1$ (melting threshold), surface atoms require:

$$T_m(r) = T_{m,\infty} \times \left[1 - \frac{f_{\text{surf}}(r) \cdot \Delta K}{K_{\text{bulk}}} \right] \tag{33}$$

For $f_{\text{surf}} \propto 1/r \rightarrow$ recover $\Delta T_m / T_{m,\infty} \propto 1/r$ ✓

6.8.2 Edge vs Surface Scaling

$r \geq 3$ **nm (Surface-dominated):**

- $N_{\text{surface}} \propto r^2$

- $N_{\text{total}} \propto r^3$
- Fraction: $f_{\text{surf}} \propto 1/r$
- $\Rightarrow \Delta T_m \propto 1/r$ ✓(observed)

$r < 3$ nm (Edge-dominated):

- $N_{\text{edge}} \propto r$ (perimeter scaling)
- Fraction: $f_{\text{edge}} \propto 1/r^2$
- $\Rightarrow \Delta T_m \propto 1/r^2$ correction appears ✓

Validation: Absence of b/r^2 improvement in $r \geq 3$ nm fits (Table 54) confirms geometric transition at 3 nm threshold.

6.9 Limitations and Outlook

6.9.1 Current Limitations

1. **Small sample size:** $N_{\geq 3\text{nm}} = 2$–6 per material
   - Statistical power limited for robust permutation tests
   - Bootstrap CIs relatively wide (10–70%)
2. **Data heterogeneity:**
   - Mix of experimental (TEM, DSC) and computational (MD) sources
   - Different synthesis methods (colloidal, gas-phase, vapor deposition)
   - Possible oxidation/contamination (especially Al, Cu)
3. **Quantum regime ($r < 3$ nm):**
   - Continuum Λ framework not designed for cluster regime
   - Electronic structure effects (HOMO-LUMO gap) not captured
   - Requires DFT or tight-binding models

6.9.2 Future Directions

1. **Expand dataset:**
   - Target $N \geq 10$ per material with $r = 3$–20 nm
   - Additional metals: Co, Ni, Pd, Sn, Bi
   - Focus on TEM + in-situ DSC for consistency
2. **Molecular dynamics validation:**
   - Direct MD calculation of $\Lambda(r, Z)$ at surfaces
   - Extract size-dependent $K_{\text{eff}}(r)$ from phonon DOS
   - Test coordination-scaling hypothesis $\alpha = 1.5 \pm 0.3$
3. **Tolman correction integration:**
   - Fit curvature-dependent $\gamma(r) = \gamma_\infty[1 + 2\delta/r]$
   - Test whether Tolman length $\delta \approx 0.1$–0.2 nm resolves discrepancies in Table 55
4. **Core-shell architectures:**
   - Predict stabilization via high-T_m shell (e.g., W-coated Au)
   - Design "anti-Gibbs-Thomson" nanoparticles for high-T catalysis

Supplementary References.

References

[1] Ledbetter, H. M. Temperature behaviour of young's moduli of forty engineering alloys. *Cryogenics* **22**, 653–656 (1982). [S22] in SI.

[2] Ogi, H. *et al.* Titanium's high-temperature elastic constants through the hcp-bcc phase transformation. *Acta Mater.* **52**, 2075–2080 (2004). [S23, S35] in SI.

[3] Blanter, M. S., Gladkii, A. V. & Smolin, L. V. Elastic properties and phase transitions in fe-n alloys at elevated temperatures. *Phys. Met. Metallogr.* **52**, 115–122 (1981). [S24] in SI.

[4] Neighbours, J. R. & Alers, G. A. Elastic constants of silver and gold. *Phys. Rev.* **111**, 707–712 (1958). [S25] in SI.

[5] Sutton, P. M. The variation of the elastic constants of crystalline aluminum with temperature between 63 k and 773 k. *Phys. Rev.* **91**, 816–821 (1953). [S26] in SI.

[6] Ledbetter, H. M. & Reed, R. P. Elastic properties of metals and alloys, i. iron, nickel, and iron-nickel alloys. *J. Phys. Chem. Ref. Data* **2**, 531–618 (1973). [S27] in SI.

[7] Varshni, Y. P. Temperature dependence of the elastic constants. *Phys. Rev. B* **2**, 3952–3958 (1970). [S28] in SI, duplicate with main paper.

[8] Kamm, G. N. & Alers, G. A. Low-temperature elastic moduli of aluminum. *J. Appl. Phys.* **35**, 327–330 (1964). [S29, S42] in SI.

[9] Gerlich, D. & Fisher, E. S. The high temperature elastic moduli of aluminum. *J. Phys. Chem. Solids* **30**, 1197–1205 (1969). [S30] in SI.

[10] Armstrong, P. E. & Brown, H. L. Dynamic young's modulus measurements above 1000°c on some pure polycrystalline metals and commercial graphites. *Trans. Metall. Soc. AIME* **230**, 962–966 (1964). [S31] in SI.

[11] Wolfenden, A. & Wolla, J. M. Mechanical damping and dynamic modulus measurements in alumina and tungsten fibre reinforced aluminium composites. *J. Mater. Sci.* **24**, 3205–3212 (1989). [S32] in SI.

[12] Ledbetter, H. M. Monocrystal-polycrystal elastic constants of a stainless steel. *Phys. Status Solidi A* **85**, 89–96 (1984). [S33] in SI.

[13] Fisher, E. S. & Renken, C. J. Single-crystal elastic moduli and the hcp $\rightarrow$ bcc transformation in ti, zr, and hf. *Phys. Rev.* **135**, A482–A494 (1964). [S34] in SI.

[14] Tanaka, K. & Koiwa, M. Single-crystal elastic constants of intermetallic compounds. *Intermetallics* **4**, S29–S39 (1996). [S36] in SI.

[15] Featherston, F. H. & Neighbours, J. R. Elastic constants of tantalum, tungsten, and molybdenum. *Phys. Rev.* **130**, 1324–1333 (1963). [S37] in SI.

[16] Bolef, D. I. & de Klerk, J. Anomalies in the elastic constants and thermal expansion of chromium single crystals. *Phys. Rev.* **129**, 1063–1067 (1963). [S38] in SI.

[17] Lowrie, R. & Gonas, A. M. Single-crystal elastic properties of tungsten from 24° to 1800°c. *J. Appl. Phys.* **36**, 2189–2192 (1965). [S39] in SI.

[18] Katahara, K. W., Manghnani, M. H. & Fisher, E. S. Pressure derivatives of the elastic moduli of bcc ti-v-cr, nb-mo and ta-w alloys. *J. Phys. F Met. Phys.* **9**, 773–790 (1979). [S40] in SI.

[19] Slutsky, L. J. & Garland, C. W. Elastic constants of magnesium from 4.2 k to 300 k. *Phys. Rev.* **107**, 972–976 (1957). [S41] in SI.

[20] Simmons, G. & Wang, H. *Single Crystal Elastic Constants and Calculated Aggregate Properties: A Handbook* 2nd edn (MIT Press, 1971). [S43] in SI.

[21] Lindemann, F. A. The melting process. *Phys. Z.* **11**, 609–612 (1910).

[22] Shapiro, S. M. Phonon anomalies and the melting of fcc metals. *Phys. Rev. B* **1**, 3982–3989 (1970). [S12] in SI.

[23] Kuramoto, E., Aono, Y. & Kitajima, K. Thermodynamic melting properties at high temperatures in some metallic glasses. *J. Phys. Soc. Jpn.* **79**, 024802 (2010). [S7] in SI.

[24] Minakov, D. V. & Levashov, P. R. Melting curves of metals with excited electrons in the quasiharmonic approximation. *Phys. Rev. B* **92**, 224102 (2015). [S10] in SI.

[25] Vopson, M. M., Rogers, N. & Hepburn, I. The generalized lindemann melting coefficient. *Solid State Commun.* **318**, 113977 (2020). [S9] in SI.

[26] Kavarnadze, T., Svanidze, E. & Svanidze, M. Ab initio calculation of the lindemann melting criterion for magnesium. *Phys. Status Solidi B* **260**, 2200452 (2023). [S19] in SI.

[27] Lawson, A. W. On the quantum theory of melting. *Philos. Mag.* **89**, 325–347 (2009). [S8] in SI.

[28] Gilvarry, J. J. The Lindemann and Grüneisen laws. *Phys. Rev.* **102**, 308–316 (1956).

[29] Jin, Z. H., Gumbsch, P., Lu, K. & Ma, E. Melting mechanisms at the limit of superheating. *Phys. Rev. Lett.* **87**, 055703 (2001). [S13] in SI.

[30] Vočadlo, L. & Alfè, D. *Ab initio* melting curve of the fcc phase of aluminum. *Phys. Rev. B* **65**, 214105 (2002).

[31] Sun, J. & Simon, S. L. The melting behavior of aluminum nanoparticles. *Thermochim. Acta* **463**, 32–40 (2007). [S15] in SI.

[32] Ross, M. & McMahan, A. K. Pressure dependence of the lindemann melting law. *Phys. Rev. B* **26**, 4088–4091 (1982). [S16] in SI.

[33] Alfè, D. Temperature of the inner-core boundary of the earth: Melting of iron at high pressure from first-principles coexistence simulations. *Phys. Rev. B* **79**, 060101(R) (2009). [S17] in SI.

[34] Morris, J. R., Wang, C. Z., Ho, K. M. & Chan, C. T. Melting line of aluminum from simulations of coexisting phases. *Phys. Rev. B* **49**, 3109–3115 (1994). [S18] in SI.

[35] Alavi, S. & Thompson, D. L. Molecular dynamics simulations of the melting of aluminum nanoparticles. *J. Phys. Chem. A* **110**, 1518–1523 (2006). [S20] in SI.

[36] Born, M. Thermodynamics of crystals and melting. *J. Chem. Phys.* **7**, 591–603 (1939).

[37] Wang, Y., Ahuja, R. & Johansson, B. Lattice instability of bcc transition metals. *Phys. Rev. B* **62**, 196–202 (2000). [S3] in SI.

[38] Forsblom, M. & Grimvall, G. How superheated crystals melt. *Phys. Rev. B* **72**, 054107 (2005). [S5] in SI.

[39] Tallon, J. L. A hierarchy of catastrophes as a succession of stability limits for the crystalline state. *Nature* **342**, 658–660 (1989).

[40] Buffat, P. & Borel, J.-P. Size effect on the melting temperature of gold particles. *Phys. Rev. A* **13**, 2287–2298 (1976).

[41] Zhang, M. *et al.* Size-dependent melting point depression of nanostructures: Nanocalorimetric measurements. *Phys. Rev. B* **62**, 10548–10557 (2000). [S2] in SI-6.

[42] Dick, K., Dhanasekaran, T., Zhang, Z. & Meisel, D. Size-dependent melting of silica-encapsulated gold nanoparticles. *J. Am. Chem. Soc.* **124**, 2312–2317 (2002). [S3] in SI-6.

[43] Zhong, J., Zhang, L. H., Jin, Z. H., Sui, M. L. & Lu, K. Superheating of ag nanoparticles embedded in ni matrix. *Acta Mater.* **49**, 2897–2904 (2001). [S4] in SI-6.

[44] Peters, K. F., Cohen, J. B. & Chung, Y.-W. Melting of pb nanocrystals. *Phys. Rev. B* **57**, 13430–13438 (1998). [S15] in SI-6.

[45] Tsuji, K., Ohshima, K. & Fujimoto, I. Electron diffraction study of melting of lead particles embedded in aluminum. *Proc. Jpn. Acad. B* **62**, 119–122 (1986). [S16] in SI-6.